Politecnico di Milano

SCUOLA DI INGEGNERIA INDUSTRIALE E DELL'INFORMAZIONE

Corso di Laurea Magistrale in Ingegneria Nucleare

TESI DI LAUREA MAGISTRALE

A novel approach to integrated Graphene Saturable Absorbers for Ultrafast Pulse Generation in an All-fibre Ring Laser Cavity

Candidato:
Giorgio Ernesto Bonacchini
Matr. 784330

Relatore:
Chiar.mo Prof. Carlo Enrico Bottani

Anno Accademico 2013–2014

"'For every complex problem there is an answer that is clear, simple, and wrong."

H. L. Mencken

"There is no object so foul that intense light will not make beautiful."

R. W. Emerson

Acknowledgments

First of all, I am really grateful to Prof. Carlo Bottani and Prof. Andrea Ferrari for giving me the unique chance to undertake this inspiring experience at the Cambridge Graphene Centre, where the entire work presented in this thesis was conducted. I must also thank my tutors, Dr. Felice Torrisi and Dr. Daniel Popa, for their constant support and trust, as well as for their patient guidance in both scientific and non-scientific matters.

This Research experience has enriched my knowledge in many fields, and I would like to acknowledge the precious help of the people who assisted me throughout this work:

- Lucia Lombardi, Flavia Tomarchio and Dr. Giulia Privitera for training me on the graphene dispersion preparation, vacuum filtration and for understanding my complicated relationship with ovens;

- Zhe Jiang and Dr. Valentin Wittwer for all the experiments related to the nonlinear optical properties of my samples and their operation in the laser cavity. I am also particularly grateful to Dr. Wittwer for his valuable insights in the world of lasers and for the useful comments on this work;

- Anna Ott for the Raman spectroscopy and statistics, and Silvia Milana for the useful discussions on the hectic life of phonons in graphene.

Along with those I have already mentioned, I would also like to sincerely acknowledge Dr. Antonio Lombardo, Dr. Matteo Bruna, Dr. Ilya Goykhman, Dr. Mari Ijas, Matteo Barbone, Domenico De Fazio. I thank all these brilliant Students and Researchers for creating an inspirational and pleasant working environment, as well as for kindly sharing with me their professional and academic experiences, thus helping me to understand what Scientific Research is, should or should not be.

Special thanks are also due to Lucia, Flavia, Giulia, Giulia, Felice, Antonio, Domenico, Matteo, Matteo, Mari, Ugo, Tiziana for making this eight-month-long experience in Cambridge enjoyable also outside the labs.

This thesis is the final step of a six-year-long journey, and I must try to express the gratitude that I feel towards all the people that bore with me for all this time:

My parents Franco and Carla, the two pillars of my life to whom this work is dedicated, for believing in me always, even when I could not do it myself.

My sister Silvia, for keeping my feet on the ground with her grumpy, adorable, sisterly love. With her, my whole family and Giovanni.

My friends in Schio, in particular Corrado, Isabella, Alberto and Maria, for being constant stars in these last ten-twenty years, and for making me feel home every time I am "back home".

Massimo and Giuseppe, whom I look up to, for their patience, support, friendship in bad (and good) times.

Alberto and Matteo, my favourite colleagues, the living proof that diversity is a never ending source of fun.

All of my friends in Torrescalla, in a random and incomplete order: Massimo, Jeanpaul, Davide "Carreiro", Raphael, Caio, Federico, Lorenzo, Lorenzo, GiorgioCarbone, Wilfried, Luca, Pietro and all the others. The years I passed in Torre were amazing: I will always cherish the memories of the moments spent together studying, playing music, talking, travelling, throwing people in the pool.

Roberto, when I first met him I could not imagine he would turn out as the best flatmate I have ever had, and a great friend too. With him, Francesca and Tommaso.

Andrea "Sonetti", and all the other members/affiliates of Flat 15.

Finally, I wish to thank Anna, for about two zillions of reasons.

Contents

List of Figures

List of Tables

Abstract

Graphene is flat monolayer of carbon atoms arranged into a two-dimensional (2D) honeycomb lattice, characterised by a wealth of optical, electronic and mechanical properties, such as high mobility and optical transparency, in addition to flexibility, robustness and environmental stability. In particular, the absence of an energy bandgap in its electronic band structure allows light absorption at all wavelengths, while the linear dispersion of the Dirac electrons enables tunability. Graphene also shows strong optical nonlinearities with ultrafast dynamics, making it a potential candidate for the fabrication of ultrafast photonic and optoelectronic devices, in particular Saturable Absorbers (SA) for the generation of ultra-short laser pulses from a continuous source.

The core objective of this thesis was to develop a novel transfer technique that would allow the integration of a polymer-free graphene film into a fibre laser cavity. Several techniques were employed in order to fully characterise the optical and electronic properties of the starting material, as well as the final photonic devices. The graphene film SA performances at high optical powers were also compared with those of graphene-PVA composites, which are currently used with success as fast SA. Finally, the graphene film SAs were tested in a fibre laser cavity operating at $\approx 1.55\ \mu$m, the most common optical telecommunications wavelength.

Liquid Phase Exfoliation (LPE) offers a simple and cost-effective pathway to fabricate graphene based photonic devices. Graphene flakes dispersions were obtained by ultrasonicating graphite in water-surfactant solutions, and then by purifying the dispersion through ultracentrifugation. The surfactants used were Sodium Cholate (SC) and Sodium Deoxycholate (SDC). Optical Absorption Spectroscopy was used to determine the concentration of graphitic material (0.235 g/L in the SC-water solution), while Raman Spectroscopy was employed to determine the doping (0.5×10^{13}cm^{-2}) and the sp^3 content (0%) of the graphene.

Several graphene films were produced by vacuum filtration, i.e. different volumes of graphene dispersion were filtered through a Nitrocellulose filter (pore

size 100nm) in order to obtain compact films with a thickness ranging from 30nm to 80nm. Firstly, these films were transferred on a quartz substrate, and their linear and nonlinear transmittance was characterised. The graphene films were also transferred on the tips of common fibre connectors, in order to integrate them in a fibre laser cavity, and their nonlinear optical properties were again assessed. Finally, graphene-PVA (Polyvinyl Alcohol) composites were produced in order to compare their behaviour at high optical powers with respect to the graphene films. The results of the characterisations suggest that graphene films are less prone to degradation when exposed to high optical powers, thus encouraging their potential exploitation in high power laser cavities.

The graphene film transferred on the tips of the fibre connectors were inserted in a Erbium Doped Fibre (EDF) laser cavity. Mode-locking regime was achieved, and ultra-short laser pulse of approximately 240fs were obtained at a repetition rate of 21MHz. The laser cavity demonstrated excellent power scaling capabilities, delivering average output powers from approximately 1mW to 16mW without losing the mode-locking condition. Higher powers could be in principle be achieved, since the upper limit of 16mW was only determined by the available pump laser diode.

Future works could approach different integration techniques for graphene produced by LPE, e.g. graphene film transfer on a D-shaped fibre, or spray-coating the graphene dispersion directly on the fibre ends. Furthermore, a variety of 2D crystals are currently being studied for their nonlinear optical properties, and many of them can be produced by LPE and thus be processed to create a new class of simple and cost-effective 2D photonic devices.

Sommario

Il grafene è un cristallo bi-dimensionale costituito interamente da atomi di carbo-
nio disposti a "nido d'ape". Tale materiale è contraddistinto da diverse proprietà
ottiche, elettroniche e meccaniche, come ad esempio alta mobilità e trasparenza
ottica, in aggiunta a flessibilità, robustezza e stabilità. La sua particolare strut-
tura a bande consente l'assorbimento di luce a tutte le lunghezze d'onda, inoltre
il grafene dimostra delle proprietà ottiche nonlineari con dinamiche ultraveloci,
le quali lo rendono un ottimo candidato per la fabbricazione di dispositivi fo-
tonici ed optoelettronici ultraveloci. Tra questi, gli Assorbitori Saturabili (SA)
consentono la generazione di impulsi laser ultracorti da una sorgente laser con-
tinua.

L'obbiettivo primario di questo lavoro di tesi consiste nello sviluppo di una
nuova tecnica di trasferimento di un film di grafene su di un connettore per fibre
ottiche; tale tecnica costituisce un nuovo metodo di integrazione di un SA in
grafene in una cavità laser in fibra ottica. Diverse tecniche sono state impiegate
per caratterizzare pienamente le proprietà ottiche del materiale nelle diverse fasi
di lavorazione. Sempre nell'ambito di questo lavoro, le prestazioni degli SA in
grafene prodotti utilizzando questa tecnica innovativa vengono comparate con
quelle ottenute sfruttando dei composti in grafene-PVA, correntemente utiliz-
zati con successo come SA in cavità laser in fibra ottica. In ultima sede, gli
SA realizzati con film di grafene vengono testati in una cavità in fibra ottica
operante a $\approx 1.55~\mu$m, la lunghezza d'onda favorita nel settore delle telecomu-
nicazioni.

L'esfoliazione da fase liquida (LPE) è un metodo semplice ed non dispendioso
per produrre il materiale di partenza con cui realizzare dispositivi fotonici. Fioc-
chi di grafene vengono dispersi in una soluzione acquosa contenente dei tensioat-
tivi, tramite l'ultrasonicazione di grafite; la dispersione viene poi purificata me-
diante ultracentrifugazione. I tensioattivi utiizzati sono Sodium Cholate (SC) e
Sodium Deoxycholate (SDC). Gli spettri di assorbimento ottico vengono utiliz-
zati per determinare la concentrazione di materiale grafitico disperso (0.235 g/L
nella soluzione contenente SC), mentre la spettroscopia Raman viene impiegata

per determinare statisticamente la concentrazione di dopanti ($0.5 \times 10^{13} \text{cm}^{-2}$) e il contenuto di difetti sp^3 (0%) dei cristalli di grafene.

Diversi film di grafene sono stati prodotti sfruttando la filtrazione a vuoto: differenti volumi di dispersione sono stati filtrati attraverso un filtro in nitrocellulosa (dimensione pori 100nm), ottenendo così dei film in grafene compatti, con spessori compresi tra i 30nm e gli 80nm. Inizialmente i film sono stati trasferiti su substrati di quarzo per consentire la caratterizzazione della loro tramittanza, sia lineare che nonlineare. Successivamente, i film di grafene sono stati trasferiti sui connettori per fibra ottica per consentire la loro integrazione nella cavità laser. In aggiunta, dei compositi di grafene-PVA (Polyvinyl Alcohol) vengono preparati per poter comparare il loro comportamento con quello dei film di grafene ad alte potenze ottiche. I risultati delle caratterizzazioni sembrano suggerire che i film di grafene degradano di meno quando esposti ad alte potenze ottiche, incoraggianddo così il loro sfruttamento in cavità laser ad alte potenze.

I film di grafene trasferiti sui connettori per fibre ottiche vengono inseriti in una cavità laser in fibra ottica (Erbium Doped Fibre). In regime di mode-locking, vengono generati impulsi ultrabrevi di circa 240fs ad una frequenza di 21MHz. La cavità laser dimostra inoltre delle notevoli capacità in termini di power scaling, mantenendo il regime di mode-locking con potenze medie in uscita comprese tra circa 1mW e 16mW. In principio, potenze più elevate potrebbero essere raggiunte dato che il limite superiore di 16mW è determinato dalla potenza di pompaggio disponibile.

Lavori futuri in questo settore potrebbero concentrarsi su diversi metodi di integrazione del grafene prodotto tramite LPE in cavità laser, per esempio trasferendo i film su fibre ottiche "D-shaped" o facendo uso di tecniche di spray-coating. Inoltre, una grande varietà di cristalli 2D sono attualmente oggetto di studio per le loro proprietà ottiche nonlineari e, poichè molti di questi possono essere prodotti sfruttando LPE, realizzando così una nuova classe di dispositivi fotonici 2D.

Chapter 1

Introduction

Since 2010, when the two scientists Andre K. Geim and Konstantin S. Novoselov were awarded the Nobel Prize in Physics, graphene has seen an increasing attention from both the industrial and the scientific communities. The enormous interest towards graphene is due to the richness of optical and electronic properties of this material. Graphene has high mobility and optical transparency, in addition to flexibility, robustness and environmental stability [9]. At the present time, research in graphene covers a wide spectrum of disciplines: from fundamental physics and chemistry, which still provide a fertile ground for applications, to device fabrication and integration [24].

In particular, the rise of graphene in photonics and optoelectronics is shown by several recent results, ranging from solar cells and light-emitting devices to touch screens, photodetectors and ultrafast lasers. These promising results are due to the combination of its unique optical and electronic properties: the absence of a bandgap allows light absorption at all wavelengths, and the linear dispersion of the Dirac electrons enables ultrawideband tunability [9]. Ultrafast laser sources, which have many existing and potential applications ranging from fundamental research to medicine, metrology, telecommunications and material processing, are among the systems the could significantly benefit from these properties [9] [30] [52]. At the current time, ultrafast pulse generation can be obtained with several different techniques, and operated in various regimes, in very dissimilar laser technologies [55]. We can anticipate that this work will focus only on passive ultrafast pulse generation through saturable absorption, in particular mode-locking in a fibre laser system operating at ≈ 1.55 μm, the most common optical telecommunications wavelength.
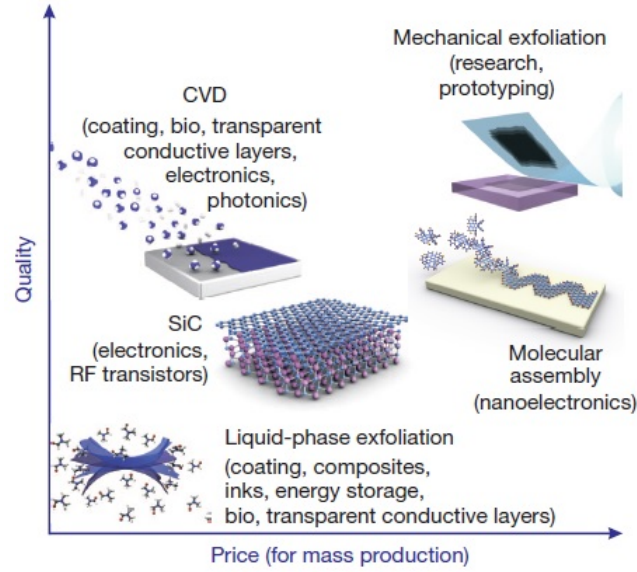
Figure 1.1: Production methods: trade-off between cost and quality. Adapted from Ref. [44]

1.1 Motivation

A vast part of ultrafast lasers exploits the nonlinear optical properties of an element called Saturable Absorber (SA) in order to turn the continuous wave output of a specific laser into a train of pulses with a duration ranging from few picoseconds to tens of femtoseconds. Currently, the most common SAs are semiconductor mirrors (SESAMs), however these require a rather complex fabrication process and packaging, and they must be properly tailored on the laser wavelength due to their narrow bandwidth (tens of nanometers). A simpler and cost-effective alternative relies on semiconducting Single Wall Nanotubes (SWNT); the diameter, and thus the energy bandgap of these nanostructures, can be chosen in order to match the laser wavelength, while the tunability of the SA is achieved by a proper choice of SWNTs' diameters distribution. This solution has proven to be functioning and reliable, however, when operating at a particular wavelength, the SWNT that are not in resonance contribute only to the losses of the cavity, thus decreasing the performance of the device [53]. Graphene, due to its wideband absorption, could cover a wide range of laser wavelengths without need for bandgap engineering [9] [53]. The techniques currently available to produce graphene are represented in Figure 1.1, which also shows how these address the cost vs. quality trade-off.

The photonic devices presented in this thesis are produced using graphene made from Liquid Phase Exfoliation (LPE); this method was preferred to the

others due to two main reasons: (i) the relatively low quality of the graphene compared to other production methods (e.g. mechanical exfoliation and CVD growth) is balanced by a fairly fast, cost effective and reliable production process [44], (ii) the material thus produced can be processed to form graphene films or graphene-polymer composite materials which have been used with success as SAs [27], [47].

Object of the work presented here is to develop a new polymer-free integration technique, able to maintain or increase the performances of the laser with respect to the results reported in literature, while keeping the same ease of processability of the graphene-polymer composites. Moreover, I will demonstrate the superior performance of the polymer-free graphene SA at high optical powers, in comparison with the graphene-PVA (Polyvinyl Alcohol) developed by Ref. [27].

1.2   Structure of the Thesis

The dissertation is organised as follows:

- Chapter 2 gives a definition of Fast SAs, proceeding thus to describe the ML process with a focus on Fast Saturable Absorber ML and Soliton formation. This is followed by an introduction of electrical, optical properties of graphene. An overview on the production and characterisation techniques used is also given.

- Chapter 3 gives a detailed description of the graphene SA preparation, and presents the results of the SA characterisation, which includes optical, spectroscopic and morphologic studies of the devices.

- Chapter 4 describes the laser cavity in which the graphene SAs are tested, and a full characterisation of the pulsed behaviour of the laser is given.

- Chapter 5 reports an alternative approach undertaken in order to integrate the graphene SA in the fibre laser cavity.

- Chapter 6 summarizes the main achievements of the research work, drawing the conclusions and mentioning possible future investigations.

Chapter 2

Graphene as a broadband fast SA for passive mode-locking

A SA is a material that shows a decreasing light absorption with increasing light intensity [30]. In this chapter I will discuss the dynamics of saturable absorption for an ideal system with two energy levels, with the double-purpose of describing the saturable absorption mechanism and obtaining a set of parameters and equations instrumental to the analysis of the graphene SA. Moreover, I will give a general description of mode-locking (ML), followed by a insight in *Passive ML* and *Soliton ML*. Finally I will describe graphene, its electronic structure, and its linear and nonlinear optical properties.

2.1 Saturable absorption

The key parameters for a SA are, in general, its frequency or wavelength range, the Modulation Depth (MD), the Saturation Fluence and its dynamic response [30]. These macroscopic parameters can be explained by considering an ideal absorber with only two energy levels separated by a energy gap. Supposing that initially only the lower level is occupied, a photon impinging on the material excites an electron from the lower to the higher energy state, provided that the photon energy matches the energy gap between the states. The excited carrier then undergoes a non-instantaneous recombination process, it eventually recombines with a hole in the lowest energy state. By progressively increasing the photon flux, the number of electrons promoted to the higher state per unit time increases consequently, until a condition of strong excitation is reached, which results in the saturation of the absorber, i.e. the initial state is depleted of electrons while the final one is almost completely occupied and it cannot accommodate new excited carriers. This condition, associated to an increase in

transmittance of the material, is a consequence of Pauli principle [55] [10].

MD is hence defined as the difference between the transmittance of the saturated absorber and its transmittance in ordinary linear behaviour:

$$MD = \Delta T \tag{2.1}$$

and saturation fluence F_{sat} is the pulse energy per unit area needed to obtain a change in transmission equal $1/e$ the MD. Moreover, the dynamics ruling the saturation of an ideal two-level absorber exposed to a pulsed laser source can be described by the following equation [31]:

$$\frac{d\alpha(t)}{dt} = -\frac{\alpha(t) - \alpha_0}{\tau_A} - \frac{\alpha(t)P(t)}{F_{sat}A} = -\frac{\alpha(t) - \alpha_0}{\tau_A} - \frac{\alpha(t)P(t)}{E_{sat}} \tag{2.2}$$

Where α_0 is the unsaturated absorption coefficient, $\alpha(t)$ is the saturable absorption coefficient that does not include non-saturable losses, τ_A is the recombination or recovery time (i.e. the time required to reduce the population on the higher state of a factor of $1/e$), $P(t)$ is the power incident on the SA, F_{sat} is the saturation fluence and A is the incident beam area.

It is possible to distinguish between slow and fast SAs: slow SAs have a recovery time which is much longer than the pulse duration (i.e.: $\Delta\tau_p \ll \tau_A$), which implies [31]:

$$\frac{d\alpha(t)}{dt} \approx -\frac{\alpha(t)P(t)}{E_{sat}} \tag{2.3}$$

This approximation yields:

$$\alpha(t)\Big|_{slow} \approx \alpha_0 \exp\left[-\frac{1}{E_{sat}} \int_0^t P(t')dt'\right] = \alpha_0 \exp\left[-\frac{E_p}{E_{sat}} \int_0^t f(t')dt'\right] \tag{2.4}$$

Where we have substituted $P(t) = E_p f(t)$, implying that, if τ_p is the time interval between two light pulses: $\int_0^{\tau_p} f(t')dt' = 1$, and E_p is the pulse energy. The overall loss that a pulse undergoes in a slow SA is [55]:

$$\alpha_p(E_p)\Big|_{slow} = \int_0^{\tau_p} \alpha(t')f(t')dt' \approx \alpha_0 \frac{E_p}{E_{sat}}\left[1 - \exp\left(-\frac{E_p}{E_{sat}}\right)\right] \tag{2.5}$$

And thus clearly not dependent of the pulse shape, but only on its amplitude. The absorbed pulse energy is subsequently: $E_{abs} = \alpha_p(E_p)E_p$.

Fast SA instead is characterised by a recovery time much faster than the pulse duration (i.e.: $\Delta\tau_p \gg \tau_A$), hence it is assumed that the absorption approximately follows $P(t)$:

$$0 \approx -\frac{\alpha(t) - \alpha_0}{\tau_A} - \frac{\alpha(t)P(t)}{E_{sat}} \tag{2.6}$$

Which in turn leads to the following expression [31] [55]:

$$\alpha(t)\Big|_{fast} \approx \frac{\alpha_0}{1 + \frac{\tau_A P(t)}{E_{sat}}} = \frac{\alpha_0}{1 + \frac{P(t)}{P_{sat}}} = \frac{\alpha_0}{1 + \frac{I(t)}{I_{sat}}} \tag{2.7}$$

Where: $P_{sat} = \frac{E_{sat}}{\tau_A}$ and $\frac{P(t)}{P_{sat}} = \frac{I(t)}{I_{sat}}$. The loss a pulse encounters in a fast SA is thus dependent on the pulse shape, and it can be analytically calculated if we assume that the SA is in the linear regime [31]:

$$\alpha(t)\Big|_{fast} \approx \frac{\alpha_0}{1 + \frac{\tau_A P(t)}{E_{sat}}} \approx \alpha_0 \left(1 - \frac{P(t)}{P_{sat}}\right) \tag{2.8}$$

The linear regime is usually valid for weak absorber saturation. By using this assumption, the loss a pulse encounters in a fully saturated ideal fast SA, for a pulse intensity $I(t) \propto sech^2(\frac{t}{\tau_p})$, is [31]:

$$\alpha_p\Big|_{fast} \approx \frac{\alpha_0}{3} \tag{2.9}$$

To summarise, I have introduced the concepts of slow and fast saturable absorption, obtaining an analytical description of these two processes in the case of an ideal two-level SA, exposed to a pulsed laser centred at a wavelength compatible with its energy bandgap, subject to only one recovery mechanism. The situation in real absorbers, e.g. in semiconductors, is obviously slightly more complex: after a strong excitation, the original Fermi-Dirac distribution of the carriers is restored by a wealth of scattering mechanisms, leading to intra-band and inter-band transitions. In Figure 2.1 it can be seen an example of how the absorption and the carrier population evolve with time in a semiconductor after an intense light pulse has impinged on the material.

Hence, strictly speaking, equation 2.2 it is only a rough approximation of the behaviour of real SAs. The main discrepancies are due to the fact that: (i) real materials are not ideal two-levels systems, but present many energy states that organize in bands, (ii) as already mentioned, more than one recovery time is usually present, and this is explained by the different intra-band relaxation and extra-band recombination mechanisms allowed in the materials. Nevertheless, even a slightly more realistic model of saturable absorption would necessarily require a computational approach rather than an analytical one, and its solutions for different materials would hardly be comparable. For this reason, it is common in literature to refer to the results just obtained for semiconductor
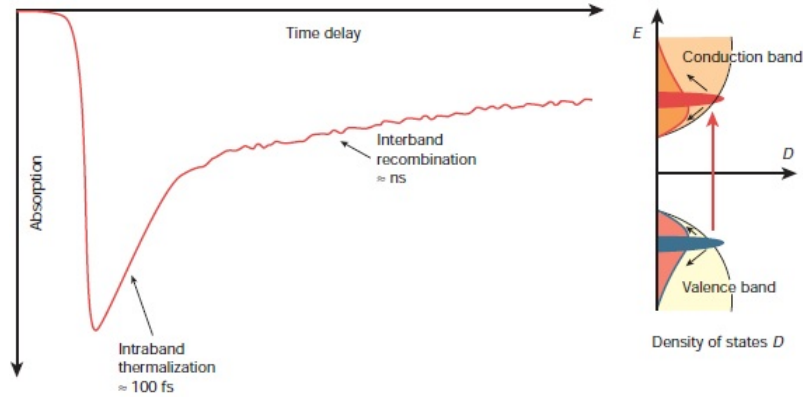
Figure 2.1: Example of absorption and carrier population evolution with time in a semiconductor: the negative peak in the absorption curve (left) corresponds to the saturation of the material which recovers thanks to intra-band and inter-band transitions. Adapted from Ref. [30].

SAs, as well as graphene ones [31] [4]. Furthermore, when the light intensity greatly exceeds I_{sat} in real absorbing materials, other nonlinear process might occur, such as two-photon absorption, free-carrier absorption, thermal and non-thermal damage [31].

Finally, I will give a very general analytical expression of transmittance for thin absorbers, following the Beer-Lambert law. Consider an light beam travelling through an absorbing medium of thickness d, in the z direction, its intensity as a function of z is:

$$\frac{dI(z)}{dz} = -\alpha I(z) \Rightarrow I(z) = I_{in} e^{-\alpha z} \tag{2.10}$$

Where it was assumed that the absorption coefficient constant along z. The intensity of the light emerging from the absorber, and thus its transmittance:

$$I_{out} = I(d) = I_{in} e^{-\alpha d} \Rightarrow T = \frac{I_{out}}{I_{in}} = e^{-\alpha d} \tag{2.11}$$

2.2 Principles of mode-locking and soliton formation in a laser cavity

Let us consider a laser resonator such as the one shown in Figure 2.2:

In general, for a sufficiently high pumping rate, it is reasonable to expect that the laser operating in CW mode will oscillate on many modes in addition to the predominant fundamental one. Under ordinary operation, the phases of these modes are randomly distributed, thus resulting in a periodic random time behaviour [55]. In Figure 2.3, an example of time behaviour of the squared
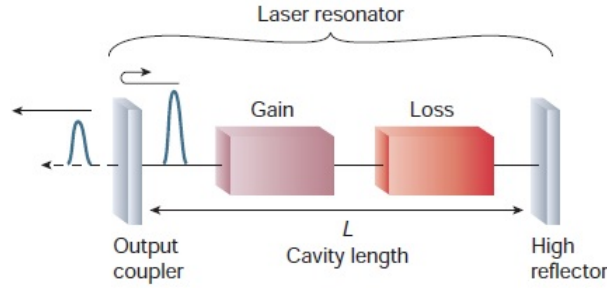
Figure 2.2: Laser cavity. Adapted from Ref. [30].

amplitude of the total electric field resulting from the superposition of $N = 31$ oscillating modes with equal amplitude but random phase.
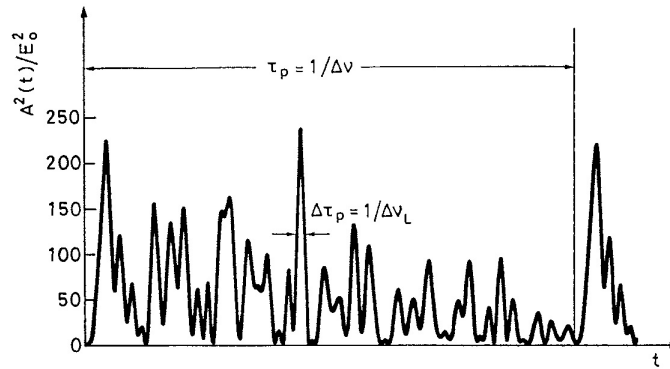
Figure 2.3: Superposition of $N = 31$ modes with random phases. Adapted from Ref. [55].

The general properties of this waveform derive directly from those of Fourier's series: (i) it is periodic with period $\tau_p = 1/\Delta\nu$, where $\Delta\nu = 2c/L$ is the frequency difference between the modes, L is the cavity length and c the speed of light in the cavity; (ii) each light pulse of the random waveform has a duration (FWHM) equal to $\Delta\tau_p \approx 1/\Delta\nu_L$, where $\Delta\nu_L = N\Delta\nu$ is the total oscillating bandwidth [55]. Considering this description, the *ML* process consists in setting a definite and constant relation between the phases of the modes, which eventually leads to the formation of a regular, pulsed waveform. Figure 2.4 represents a train of pulses obtained by superimposing seven oscillating modes with equal intensity and phase difference locked according to the relation:

$$\varphi_i - \varphi_{i-1} = const \qquad i = 1, 2, ..., 7 \tag{2.12}$$

The total electric field, for the general case of $2n + 1$ modes, is [55]:

$$E(t) = A(t)e^{j2\pi\nu_0 t} \tag{2.13}$$
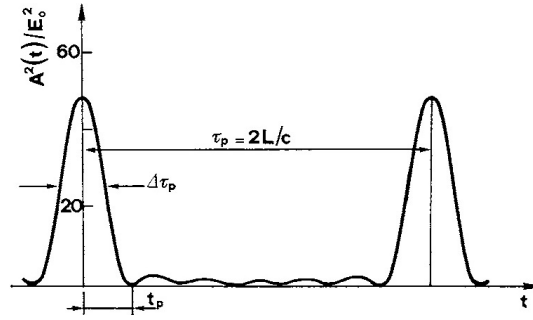
Figure 2.4: Superposition of 7 modes with equal amplitude E_0 and locked phases. Adapted from Ref. [55].

Where ν_0 is the centre-mode frequency and $A(t)$ is the time dependent amplitude (assuming that the phase of the central mode is zero) [55]:

$$A(t) = E_0 \frac{\sin\left[(2n+1)\,2\pi\Delta\nu t/2\right]}{\sin\left[2\pi\Delta\nu t/2\right]} \tag{2.14}$$

The previous equations considered the superposition of modes with equal amplitude E_0, however a more realistic approximation makes use of a bell-shaped envelope of the mode spectrum. In particular, for a Gaussian spectral distribution, the time dependent intensity of the pulses is also a Gaussian function of time [55]:

$$A(t)^2 \propto \exp\left[-\left(\frac{2t}{\Delta\tau_p}\right)^2 \ln 2\right] \tag{2.15}$$

Where: $\Delta\tau_p = 2\ln 2/\pi\Delta\nu_L = 0.441/\Delta\nu_L$, both considered at FWHM. Hence it is possible to summarize the discussion by saying that, when the mode-locking condition 2.12 applies, the electric field amplitude is calculated as the Fourier transform of the spectral amplitude. In this case, the pulse width is related to the laser spectral bandwidth with a relation of the kind:

$$\Delta\tau_p = \beta/\pi\Delta\nu_L \tag{2.16}$$

Where β is a numerical factor which depends on the shape of the spectral distribution of the modes' amplitudes. When a pulse of this sort is measured, it is said to be *transform-limited* [55].

After considering the effects of ML on the laser behaviour, it is possible to proceed to explain which techniques can be used to obtain this regime. The methods of ML can be divided in two categories: Active ML, in which the process is driven by a source external to the cavity, and Passive, which makes use of an internal element that exhibits inherent nonlinear optical properties that lead
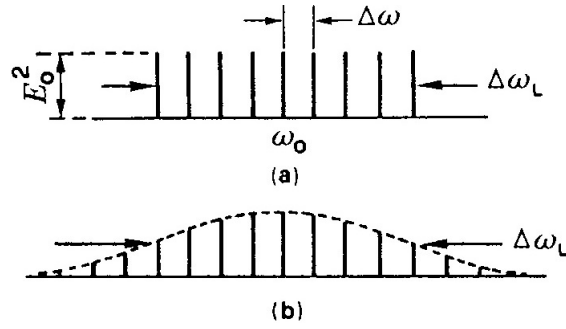
Figure 2.5: Mode amplitudes (vertical lines) versus frequency for a ML laser. (a) Uniform and (b) Gaussian amplitude distributions. Adapted from Ref. [55].

to the locking of the modes. Passive ML can also be divided in different types, however those relevant to our discussion are *Fast SA ML* and *Soliton ML*.

2.2.1   Fast saturable absorber mode-locking

Let us consider a laser cavity that includes a SA which initially produces the waveform shown in Figure 2.3. The light bursts randomly distributed will be mostly absorbed by the SA, but the most intense one will suffer the least attenuation due to the absorption saturation. After many round trips this pulse can increase its intensity and thus become less and less subject to attenuation. If the round-trip power gain of the laser is initially roughly equal to the cavity losses, saturable absorption creates a time window of positive net gain coincident with the pulse passage through the SA, as shown in Figure 2.6:
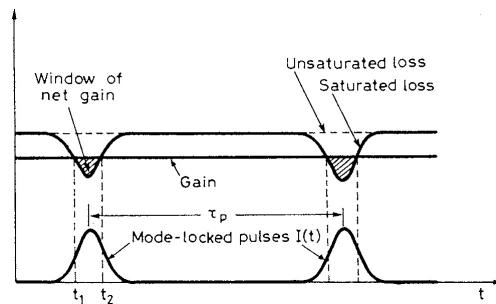
Figure 2.6: Passive ML by fast SA. Adapted from Ref. [55].

This mechanism by itself would lead to a progressively shorter pulse, the pulse tails seeing a net loss while the peak a net gain, however a steady state condition is established between the pulse shortening and its broadening due to the finite bandwidth of the gain medium [55]. This steady state condition usually turns out to give a pulse amplitude described by a hyperbolic secant function:

$$E(t) \propto sech(t/\tau_p) \tag{2.17}$$

In the case of fibre lasers, a SA main role is that of starting the ML and to stabilise the pulsed waveform, which is in fact due to the formation of a soliton, which is a wave that maintains its shape while travelling at constant speed along the cavity [29] [18]. The presence of a soliton in a resonant structure such as a laser cavity arises when a balance between the effects of Self-Phase-Modulation (SPM) and anomalous Group-Velocity-Dispersion (GVD) occurs [55] [31]. A clearer understanding of this balance can be obtained by reporting the definitions of GVD and SPM.

2.2.2   Soliton mode-locking

Let us first consider a linearly polarized, monochromatic electro-magnetic wave at frequency ω_L propagating along the z direction of a transparent medium [55]:

$$E(z,t) = A_0 e^{j(\omega_L t - \beta_L z)} \tag{2.18}$$

Where the amplitude A_0 is constant and the wave-vector β is usually a function of the frequency ω and depends on the medium. The group velocity of a wave travelling through the medium is defined as:

$$v_g = \left(\frac{d\omega}{d\beta}\right)_{\beta_L = \beta(\omega_L)} \tag{2.19}$$

Where $\omega = \omega(\beta)$ is the dispersion relation of the medium. The GVD is defined as:

$$\beta_2 = \left(\frac{d\beta^2}{d^2\omega}\right)_{\omega_L} = \left[\frac{d}{d\omega}\left(\frac{1}{v_g}\right)\right]_{\omega_L} \tag{2.20}$$

Whose magnitude represents the pulse broadening in time per unit length per unit frequency. The expression above tells us that, if GVD (β_2) is non-zero, different spectral regions of a pulse will travel with different group velocities in the medium, thus broadening the pulse in time. If GVD is positive, low frequency components will travel faster than the low ones, and vice versa if it is negative[55]. Let us now examine a light pulse with spectrum centred around ω_L travelling along the z direction of a medium that shows the optical Kerr effect, i.e. the refractive index depends on the light intensity profile $n = n(I)$; the phase of the electro-magnetic wave is:

$$\varphi = \omega_L t - \beta_L z = \omega_L t - \frac{\omega_L n(I)}{c} z \,. \tag{2.21}$$

This implies that, since the intensity is time dependent, the instantaneous frequency of the travelling wave changes with time as well:

$$\omega = \frac{\partial(\omega_L t - \beta_L z)}{\partial t} = \omega_L - \frac{\omega_L z}{c} \frac{\partial n(I)}{\partial t} = \omega_L - \frac{\omega_L n_2 z}{c} \frac{\partial I}{\partial t} \tag{2.22}$$

Where in the last passage it is assumed that: $n = n_0 + n_2 I$ [30] [55].
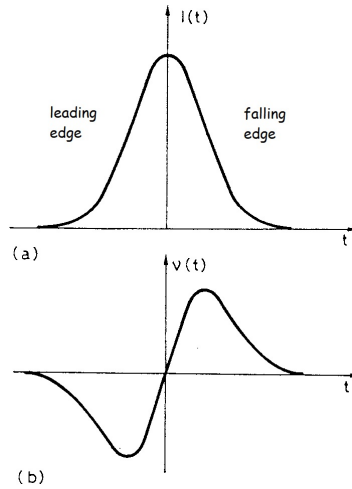
Figure 2.7: Self-Phase-Modulation. (b) Behaviour of the pulse frequency versus time when a light pulse (a) travels through a medium exhibiting optical Kerr effect. Adapted from Ref. [55].

The phase of the pulse is thus linearly dependent on the negative time derivative of the intensity. This effect is called SPM, and it can be easily visualised considering Figure 2.7. The overall effect on the pulse is that its leading edge shifts towards lower components of the spectrum, while the opposite occurs for the back of the pulse. It is now clear how a medium showing negative GVD is conducive in compressing the pulse: the leading edge of the pulse, shifting towards lower frequencies, is slowed down, while the back of the pulse, which move towards higher frequencies, becomes faster.

2.3   Graphene

The objective of this section is to describe the physical and electronic band structure of graphene, the latter being of primary importance as a starting point for the understanding of graphene's solid-state properties. For the sake of clarity, the description will only cover the physical properties which are relevant

to this work, and which justify and encourage the use of graphene as a broadband fast SA.

2.3.1 Lattice

Graphene is a flat monolayer of sp^2 hybridised carbon atoms, arranged in Bravais lattice with two atoms per basis, also known as *honeycomb* lattice [24][63][43]. Figure 2.8c shows a schematic representation of the sp^2-hybridised carbon atom: in graphene, the sp^2 orbitals of two different atoms in the lattice interact, resulting in strong and highly localised covalent bond called σ, while the $2p_z$ electrons form the π-bonds, which are weakly bound to their original nuclei and thus form a distributed electron cloud. A representation of the honeycomb lattice with other possible sp^2 allotropes of graphene is shown in Figure 2.9.
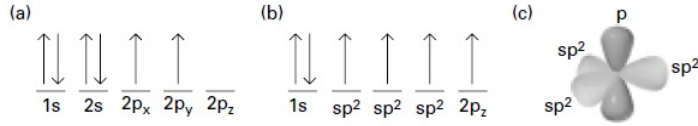
Figure 2.8: Disposition of electrons in (a) elemental C, (b) sp^2 hybridised C. (c) Representation of the sp^2 and p$_z$ atomic orbitals. Adapted from Ref. [63].

The primitive unit cell of graphene hexagonal lattice is an equilateral parallelogram with side $a = a_{C-C}\sqrt{3} \approx 2.46$Å, where $a_{C-C} \approx 1.42$Å is the C-C bond length [63]. The primitive unit vectors, as depicted in Figure 2.10a are:
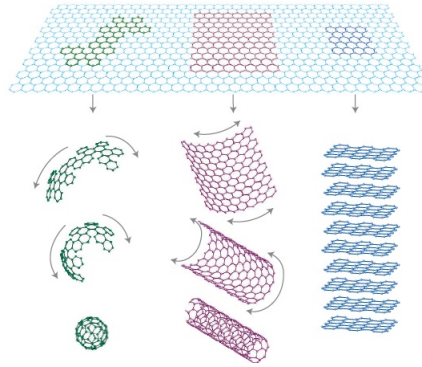
Figure 2.9: Carbon allotropes of graphene: fullerenes, nanotubes and graphite. Adapted from Ref. [24].

$$\boldsymbol{a_1} = \left(\frac{a\sqrt{3}}{2}, \frac{a}{2}\right) \qquad \boldsymbol{a_2} = \left(\frac{a\sqrt{3}}{2}, -\frac{a}{2}\right) \tag{2.23}$$

Where: $|\boldsymbol{a_1}| = |\boldsymbol{a_2}| = a$.
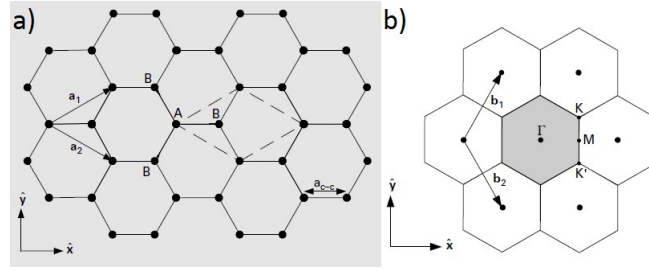
Figure 2.10: Graphene direct (a) and reciprocal (b) lattice. Adapted from Ref. [63].

The reciprocal lattice is also an hexagonal lattice, but rotated of 90° with respect to the direct one. The reciprocal lattice primitive vectors, defined by the First Brillouin Zone (FBZ), are:

$$\boldsymbol{b_1} = \left(\frac{2\pi}{a\sqrt{3}}, \frac{2\pi}{a} \right) \qquad \boldsymbol{b_2} = \left(\frac{2\pi}{a\sqrt{3}}, -\frac{2\pi}{a} \right) \tag{2.24}$$

Where: $|\boldsymbol{b_1}| = |\boldsymbol{b_2}| = 4\pi/a\sqrt{3}$.

The Γ-point is the centre of the FBZ, while K, K' and M are the other high-symmetry points. It is important to state that K and K' are essentially equivalent, but a distinction is often made as it is convenient when electron-phonon scattering mechanisms are studied [63].

2.3.2   Electronic band structure and density of states

The electronic band structure of the material can be obtained with different techniques [63]. Sophisticated *ab-initio* calculations yield the band structure shown in Figure 2.11, which clearly depicts the formation of bonding, σ and π, and anti-bonding, σ^* and π^*, energy branches related to the σ and π electrons discussed in section 2.3.1.
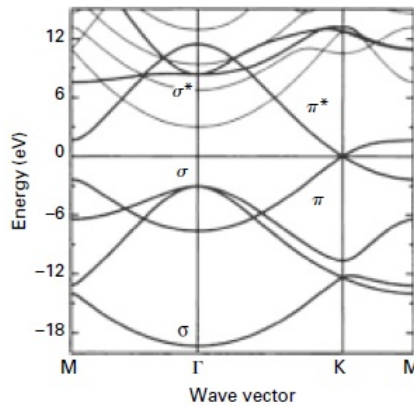
Figure 2.11: *Ab-initio* band structure of graphene. Adapted from Ref. [63].

Indeed, the time-independent 3D Schroedinger equation can be solved analytically by using the Tight-binding approximation [63][43]. This approach, compared to the computational one, has the only advantage of giving a clearer qualitative description of the behaviour of the π and π^* bands in the proximity of the K point, which is at the basis of most of graphene's peculiar optical and transport properties. By making use of the following approximations, it is possible to obtain an analytical solution: (i) the Nearest Neighbour Tight-binding (NNTB) model and (ii) Electron-hole symmetry, which yield [63]:

$$E(\boldsymbol{k})^{\pm} = \pm\gamma\sqrt{1 + 4\cos\frac{\sqrt{3}a}{2}k_x \cos\frac{a}{2}k_y + 4\cos^2\frac{a}{2}k_y} \qquad (2.25)$$

k_x an k_y being the components of the total wavevector of the FBZ. In literature, γ is referred to as *nearest neighbour overlap energy*, *transfer energy* or *Carbon-Carbon interaction energy* (typical values $2.9 - 3.1$eV).
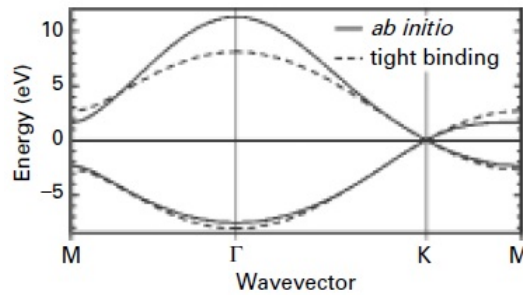
Figure 2.12: Comparison of *ab-initio* and NNTB calculations for graphene, with the further assumption of electron-hole symmetry. Adapted from Ref. [63].

Figure 2.12 shows a comparison of the analytical and numerical models mentioned. The two different approaches provide consistent results in the proximity of the K (and K') point of the FBZ, where we notice a contact between the bonding π and anti-bonding π^* bands, also known as valence and conduction bands of the material, in analogy with semiconductors. Moreover, by calculating the number of states of the valence band, it is possible to determine that the position of the Fermi energy E_F is exactly where the valence and conduction bands meet. These two peculiarities, the absence of a bandgap and the position of E_F, tell us that graphene is a special semimetal or zero-gap semiconductor, whose Fermi sphere (which in a 2D lattice is actually a circumference) reduces at the K points of the FBZ [63][43], also known as Dirac points, for reasons explained in the following paragraph.

Furthermore, by expanding equation 2.25 in the proximity of K and K' points around E_F, we find a linear dispersion relation for both the conduction

and valence bands [63][43]:

$$E(\boldsymbol{\kappa})^{\pm} = \pm\hbar\nu_F \mid \boldsymbol{k} \mid \tag{2.26}$$

Where $\boldsymbol{\kappa} = \boldsymbol{k} - \boldsymbol{K}$ is the wavevector around the K (K') point, and $\nu_F = (1/\hbar)\nabla_{\boldsymbol{k}}E = \sqrt{3}\gamma a/(2\hbar) \approx 10^6$m/s is the Fermi velocity. The linear relation expressed by equation 2.26 is of utmost relevance for understanding graphene's transport properties: this particular dispersion, only valid at energies close to E_F (±0.6eV) [63], is characteristic of so-called massless particles (particles with zero effective mass), which are usually described by Dirac's relativistic quantum mechanical wave equation rather than Schroedinger's. The implications of this result are reflected for example in an estimated mobility (μ) of up to 10^6cm^2/Vs in suspended samples. In Figure 2.13 it is represented the band structure of graphene: the linear dispersion around K results in the characteristic shape called Dirac cone.
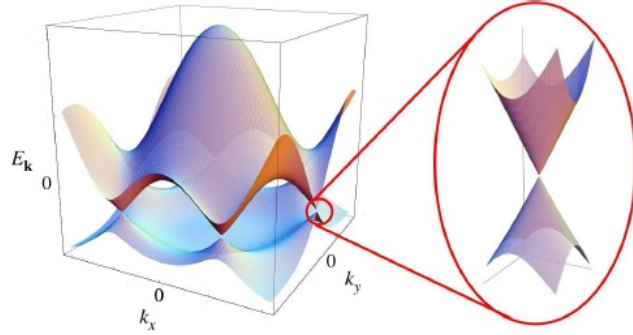
Figure 2.13: 3D representation of graphene band structure, with a close view of the Dirac point. Adapted from Ref. [43].

The Density of States for graphene in the proximity of the Dirac point can now be calculated:

$$D(E) = \frac{dN(E)}{dE} \tag{2.27}$$

Where $N(E)$ is the number of energy states with energy between 0 and E which, in a 2D system of surface area Ω, can be calculated as:

$$N(E) = 2g_z\frac{\pi|\boldsymbol{k}|^2}{2\pi/\Omega} = \frac{2\Omega}{\hbar\nu_F}E^2 \tag{2.28}$$

Where we have exploited the linear dispersion 2.26 and accounted for the spin degeneracy as well as the zone degeneracy ($g_z = 2$). Combining equations 2.27 and 2.28 a linear DOS is obtained:

$$D(E) = \frac{4\Omega}{\hbar \nu_F} E \tag{2.29}$$
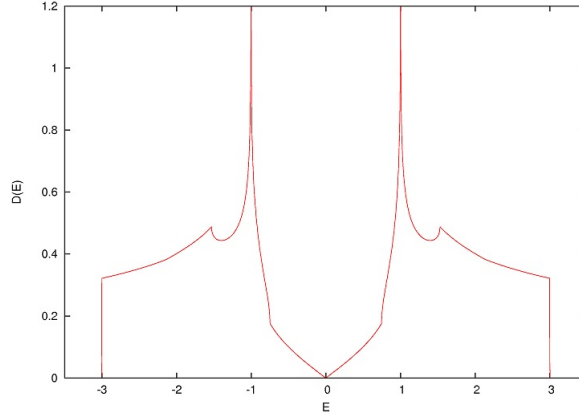
Figure 2.14: Graphene DOS as calculated by Ref. [34].

Figure 2.14 shows the complete DOS of graphene, which is consistent with equation 2.29 for energy values close to the Fermi level. The two peaks shown at $\approx \pm 1$ in the energy scale of Figure 2.14 are *van Hove* singularities [2]. It can also be noted that at the Fermi energy the DOS vanishes to zero even though there is no bandgap. This is the reason why graphene is considered a semi-metal in contrast to regular metals that have a large DOS at the Fermi energy [63].

2.3.3   Graphene as a broadband fast SA: linear and nonlinear optical properties
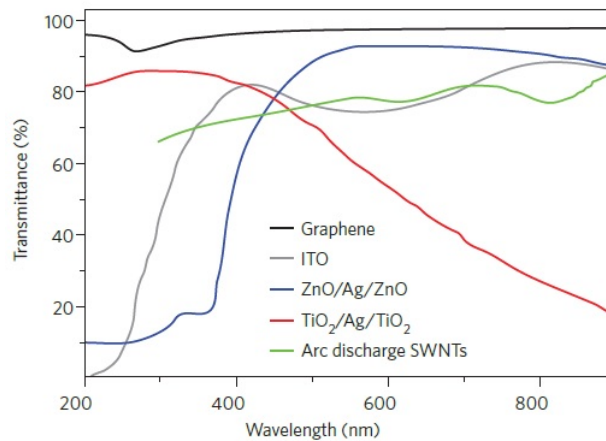
Figure 2.15: Transmittance of graphene compared to those of other transparent conductors: it is almost flat over a wide spectrum, with the exception of the negative peak at ≈ 270nm due to the van Hove singularities. Adapted from Ref. [9].

In the previous section the lattice, the electronic band structure and the DOS of graphene were presented. The most relevant points for our concerns can be summarised in three considerations: (i) in graphene, the π bonding and π^* anti-bonding bands touch at the K point of the FBZ; (ii) the Fermi level of an ideal graphene layer is positioned exactly where the two mentioned bands touch, that is at the Dirac point; (iii) the dispersion relation for the electrons close to the Fermi energy (± 0.6eV) is linear, and thus is also the DOS of the material. The consequences of these peculiarities are reflected in the remarkable optical properties of the material: the optical absorption of graphene is truly broadband, being almost flat from 300 to 2500nm, with a peak in the UV region (≈ 270nm) due to the exciton-shifted van Hove singularity in the graphene DOS (Figure 2.15)[42] [32]. The transmittance of a Single Layer Graphene (SLG) can be expressed by applying Fresnel equations in the thin-film limit for a material with a fixed universal optical conductance [33] $G_0 = e^2/(4\hbar) \approx 6.08 \times 10^{-5} \ \Omega^{-1}$, as:

$$T = (1 + 0.5\pi\alpha)^{-2} \approx 1 - \pi\alpha \approx 97.7\% \qquad (2.30)$$

where $\alpha = e^2/(4\pi\epsilon_0\hbar c = G_0/(\pi\epsilon_0 c) \approx 1/137$ is the fine-structure constant [42]. The optical absorption of a Single Layer of Graphene is thus 2.3% over the visible spectrum (Figures 2.15 and 2.16). The interaction of light with two or more graphene layers superposed on each other should also be considered, as it is common during experimental activities to deal with these systems rather than SLG: Few Layer Graphene (FLG) can be considered as a superposition of almost non-interacting SLG, acting as two-dimensional electron gases with little perturbation from the adjacent layers. Since graphene only reflects $< 0.1\%$ of the incident light in the visible region, rising to $\approx 2\%$ for ten layers [14], the optical absorption of FLG is thus proportional to the number of layers, each one absorbing 2.3% of visible light over the whole visible spectrum.

The nonlinear optical properties of graphene have been investigated in several studies using time-resolved characterisation techniques. *Pump-probe spectroscopy* is a particularly valuable tool to determine the carriers' relaxation time constants mentioned in section 2.1, or in general to study the ultrafast nonequilibrium carrier dynamics [11] [13] [12] [57]. The photo-excited carrier dynamics in graphene is presented in Figure 2.17. At first, when an ultrashort laser pulse impinges on the material, it creates a strongly out-of-equilibrium (non-thermal) distribution of electrons and holes in valence and conduction bands (the narrow peaks in Figure 2.17b). Subsequently, the peaks broaden due to electron-electron collisions, converging towards hot Fermi-Dirac distributions on a time
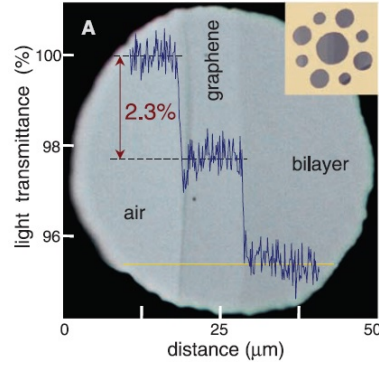
Figure 2.16: Photograph of a 50 μm aperture partially covered by SLG and BLG. The line scan profile shows the intensity of transmitted white light along the yellow line. (Inset) Sample design: a 20 μm-thick metal support structure has several apertures of 20, 30, and 50 μm in diameter with graphene crystallites placed over them. Adapted from Ref. [42].

scale of $\tau_1 \lesssim 15$fs. On a slightly longer time scale, approximately $150 - 170$fs (τ_2), hot-electrons cooling by interaction with optical phonons predominates. Finally, electrons thermalise with a relaxation time constant $\tau_3 > 1$ps thanks to anharmonic decay of hot phonons [13].
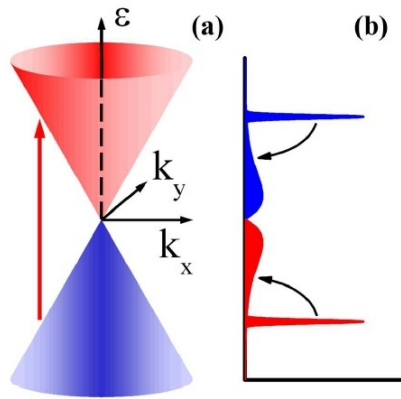
Figure 2.17: (a) The momentum conserved photon absorption process in graphene; (b) Instantaneous photon absorptions generate nonequilibrium distributions of electrons (**blue**) and holes (**red**), which subsequently thermalise through ultrafast intraband carrier-carrier and carrier-optical phonon scattering to form Fermi-Dirac distributions. Adapted from Ref. [64].

In the light of these considerations, the sense of the model presented in section 2.1, which makes use of only one relaxation time (τ_A in equation 2.2), must be clarified. As already mentioned, equations 2.4 and 2.7 are only rough approximations of the real behaviour of a SA for two main reasons: (i) real materials are not ideal systems and (ii) more than one recovery time is usually present, as in the case of graphene [11] [13] [12] [57]. However, as already

discussed, these expressions allow a convenient and fast way to interpret the experimental results and are thus commonly used. Nevertheless, the three time constants (τ_1, τ_2, τ_3) cover a wide range of values, from tens of femtoseconds to picoseconds, and this fact could in principle raise the question whether graphene actually operates as a fast SA. In section 2.1 it is shown that the definition of fast SA relies on the duration of the laser pulse in the cavity, and it will be shown later that the pulse durations achieved in our laser cavities are of the same order of magnitude of τ_2, thus implying that graphene does not fully conform to the definition of fast SA. However, it is again important to remind that equations 2.4 and 2.7, which are founded on this definition, are just a convenient approximation when a rather immediate interpretation of experimental results is needed.

2.4 Graphene Production Methods

Several production techniques are available for the fabrication of graphene, as shown in Figures 1.1 and 2.18. In particular, Liquid Phase Exfoliation (LPE) of graphite [28][36], micromechanical cleavage [45] and Chemical Vapour Deposition (CVD) [3] [48] have been demonstrated for SAs in different studies [27] [38] [9].
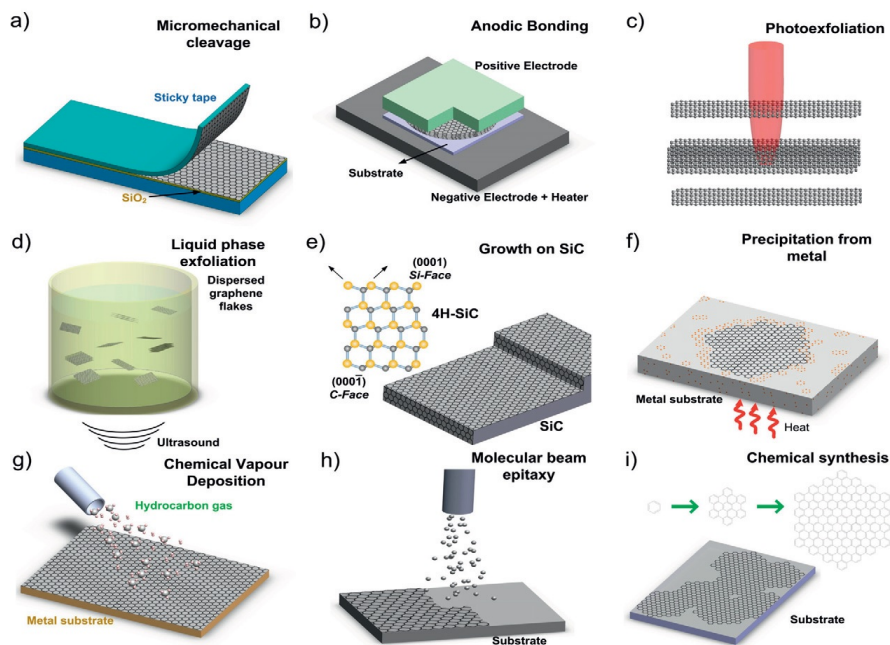
Figure 2.18: Schematic illustration of the most relevant graphene production methods. Adapted from Ref. [7].

   Graphene can be isolated by micromechanical cleavage of graphite by means
of adhesive tape (so called *scotch-tape* technique) [45]. This method gives the
best samples in terms of purity, defects, mobility and optoelectronic proprieties,
but is not good for mass production since the flakes' maximum size is limited
to few millimetres [9]. On the other side, high-quality, large-area, SLG and
FLG sheets can also be synthesized on various substrates at ambient pressure
by using hydrocarbons at suitable temperatures in a CVD reactor. This process
enables a high-throughput growth of graphene over large areas compared to
the scotch-tape technique [3], ensuring also a good material quality. I will
now concentrate on LPE because, among the exfoliation techniques, it offers
advantages in terms of scalability, cost and it does not require expensive growth
substrates. Furthermore it is an ideal means to produce the starting material
for thin films and composites [26] for optoelectronics and photonic applications
[53] [26].
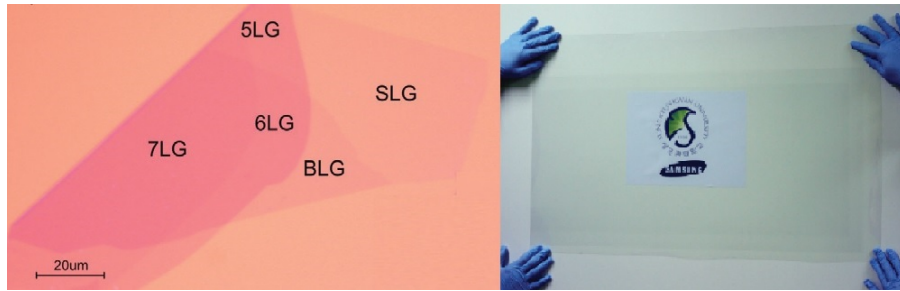
Figure 2.19: Samples of micromechanically cleaved (**left**) and CVD grown (**right**)
graphene. Adapted from Ref. [7].

2.4.1   Liquid Phase Exfoliation of graphite in water-based solutions

Graphite can be exfoliated by chemical wet dispersion in a mild ultrasonication
bath (in this work of thesis: Branson 450A, 25W of power, 8-10°C), both in aqueous [36] and non-aqueous solvents [28], the former being of prime interest for
photonics applications [26]. The exfoliation process is governed by the balancing between the energy required to exfoliate graphite and the solvent-graphene
interaction. Stable dispersions require the Gibbs free energy of mixing, ΔG_{mix}
, to be zero or negative [25], hence:

$$\Delta G_{mix} = \Delta H_{mix} - T\Delta S_{mix} \leq 0 \qquad (2.31)$$

   T being the temperature, ΔH_{mix} the enthalpy of mixing and ΔS_{mix} the
entropy change in the mixing process. For graphene, ΔS_{mix} is small, being the

main contribution due to Van der Walls forces [28]. Therefore, for dispersion and stabilisation of graphene in solvents, ΔH_{mix} needs to be very small [25]. This can be achieved by choosing a solvent whose surface energy is very close to that of graphene [28]. The surface energy of NMP (N-Methyl-2-pyrrolidone) and other pure amide solvents (DMF, DMA, etc.), for example, satisfies this requirement and allows efficient exfoliation of graphite [28]. Water, on the other hand, has a surface tension that is too high (≈ 72 mJ/m^2 [35]) to match the surface energy of graphite; for this reason, exfoliation of graphite flakes is achieved in a water-surfactant assisted solution [36].

Once the thermodynamic condition presented in equation 2.31 is met, mechanical energy must be supplied to the mixture by ultra-sonication in order to disrupt the weak π-π interactions (Van der Waals forces) between different graphitic planes while the adsobed surfactants stabilise the repulsion between hydrophobic carbon surface and water, preventing subsequent re-aggregations. It is thus crucial to determine which surfactants present the highest efficiency in this process and also to accurately understand the encapsulating process. The molecules that so far have demonstrated positive results when used as surfactant in aqueous solutions are shown in Figure 2.20.
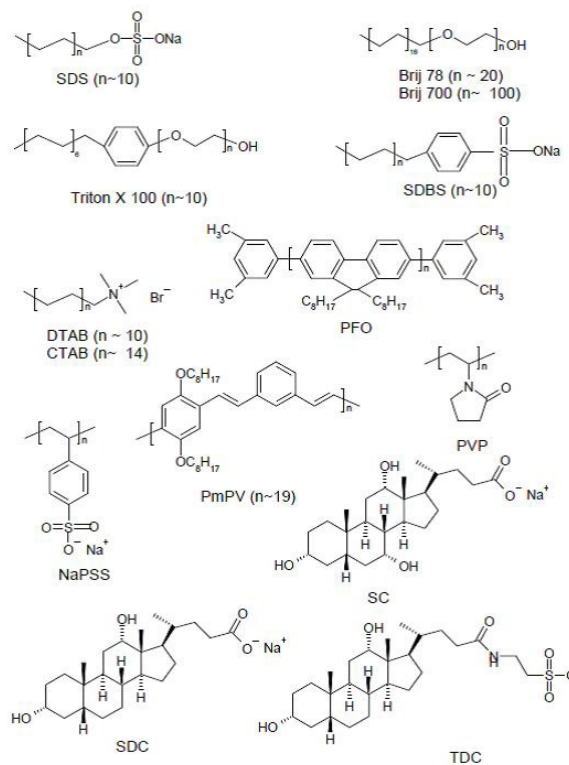
Figure 2.20: Chemical structures of some commonly used surfactants and polymers for dispersion in aqueous and organic solvents. Adapted from Ref. [6].

At the end of the exfoliation process, the dispersions contain a variety of graphitic materials, ranging from SLGs and FLGs to more bulky graphite flakes. For this reason the dispersions are ultracentrifuged using a TH-641 swing rotor in a Sorvall WX-100 Ultracentrifuge, and only the resulting top 70% is kept for further use. This purification process is known as Sedimentation Based Separation (SBS), and it consists in dividing the various particles dispersed in the solution on the basis of their sedimentation rate, which arises as a consequence of a centrifugal force.
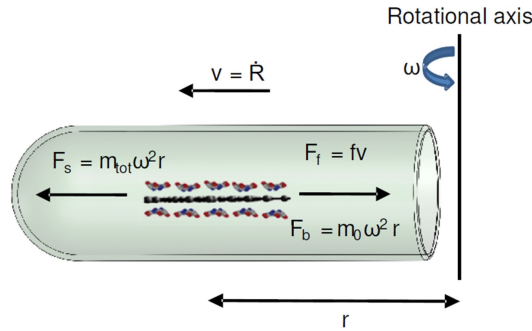
Figure 2.21: Force field acting on a SLG encapsulated by surfactant molecules in an ultracentrifugation cell during ultracentrifugation with a swinging bucket rotor. Adapted from Ref. [58].

In Figure 2.21, the three forces acting on a SLG encapsulated by the surfactant molecules are represented: (i) the centrifugal force $F_S = m_{tot}\omega^2 r$, (ii) the buoyant force $F_b = m_0\omega^2 r$ (Archimede's Principle) and (iii) the frictional force $F_f = -fv$, where m_{tot} and m_0 are the masses of the SLG encapsulated and of the displaced fluid, ω is the angular velocity, r the distance from the rotational axis and finally v and f are the radial velocity and the friction coefficient. Generally, a particle in a medium of constant density will be accelerated under a centrifugal field, until the net force on the particle equals the force resisting its motion through the medium. The friction coefficient depends on the shape and on the size of the particles and it increases as the particle geometry moves away from a spherical shape, which means that large or elongated particles experience more frictional drag than compact spherical ones having the same mass. Both F_b and F_f act in the opposite direction to the sedimentation, as shown in Figure 2.21 [62] [51]. The rate of sedimentation in a centrifugal field is described by the Svedberg equation [54]:

$$s = \frac{v}{r\omega^2} = (1 - \overline{v}\rho)\frac{m_{tot}}{f} \qquad (2.32)$$

where s is the sedimentation coefficient, commonly reported in Svedberg [S]

unit, where 1S corresponds to 10^{-13}s, v is the sedimentation velocity, $\overline{v}$ is the partial specific volume (the volume in ml that each gram of the solute occupies in solution) and ρ is the density of the solvent [g/ml]. The sedimentation coefficient depends on the properties of the particle and it is proportional to its buoyant effective molar weight, while it is inversely proportional to f [54]. As the concentration of graphitic material on the bottom of the centrifuge pipe increases, the diffusion process opposes further sedimentation [54] [62]. Equilibrium is reached when sedimentation and diffusion are balanced and the concentration of flakes along the cell no longer changes with time. As reported in the above equation, at the equilibrium the sedimentation of the material only depends on the frictional coefficient and on the molecular weight. Thus, the SBS of SLGs and FLGs ensures a separation based on molecular weight and shape and produces flakes with lateral sizes ranging from few nanometres to a few micrometres, starting with concentrations up to a few g/l.

In Figure 2.22 shows a summary of the dispersion preparation process.
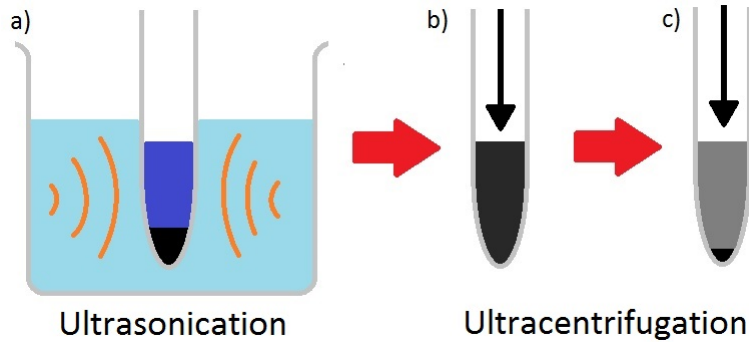
Figure 2.22: Dispersion preparation process, from ultrasonication to ultracentrifugation.

2.4.2   The role of surfactants in the LPE of Graphene

Previous studies have assessed that, among most common surfactants, the chemicals that allow a more efficient and stable dispersion of graphene in water are bile salts, i.e. trihydroxy bile salt Sodium Cholate (SC) and dihydroxy bile salt Sodium Deoxycholate (SDC) [58].

Figure 2.23 shows a representation of the two molecules that clearly shows their amphiphilic nature: the α side is hydrophilic thanks to the hydroxyl groups, while the β side is hydrophobic and thus it is the one bonding to graphene sidewalls. The advantage of bile salts on other surfactants, e.g. Sodium Dodecylbenzene Sulfonate (SDBS, in Figure 2.20), is their relatively large hydrophobic contact area per molecule ($1.8-3\text{nm}^2$) which leads to a better adsorp-
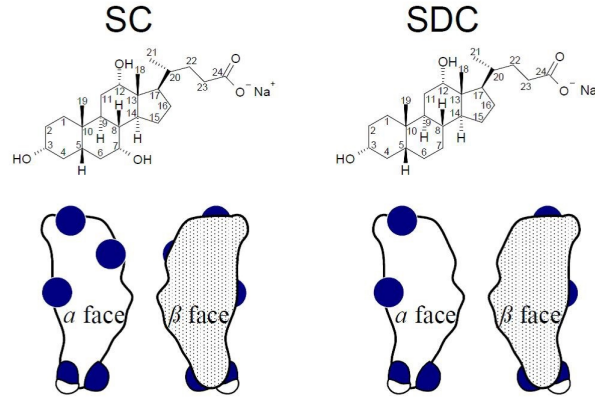
Figure 2.23: Molecular structures (**top**) and schematic model (**bottom**) of SC and SDC bile salts. Adapted from Ref. [58].

tion to the graphitic planes [27]. In fact, hydrophobicity rules the adsorption process of the molecules on the graphitic surfaces, and it is measured by the Hydrophobic Index [41]:

$$HI = HI_A + HI_B \qquad (2.33)$$

Where A and B are two anomers:

$$HI_{A(B)} = \frac{Hydrophobic\,Area_{A(B)}}{Hydrophilic\,Area_{A(B)}} \times \%anomer_{A(B)} \qquad (2.34)$$

Looking at the structure of SDC and SC they differ only in the number of the hydroxyl groups. The lack of the hydroxyl group in position $\alpha 7$ increases the hydrophobic area, and thus the HI of deoxycholic acid (7.27) is higher than its trihydroxy counterpart, cholic acid (6.91) [41]. This also result in a different coverage of the flake surface. In the case of SC, the presence of the hydroxyl group in position $\alpha 7$ on the hydrophilic part, reduces the hydrocarbon-water contact area by $30 - 40\%$ as compared to the dihydroxy species, i.e. SDC [49] [27]. This last consideration suggests that SDC is a more efficient surfactant than SC in delivering a higher concentration of dispersed material as well as a higher yield of SLG [27]. In this work however, as I will show in Chapter 3, the concentration of graphitic material dispersed in the SC-water solution was about three times higher than the one prepared with SDC.

2.5   Optical characterisation techniques

The following section will give an overview on the characterisation techniques adopted in this work, namely Optical Absorption Spectroscopy (OAS), Raman

Spectroscopy and Nonlinear Optical Absorption. The combination of these three techniques gives access to the most relevant quantities necessary to determine the properties of the starting material as well as the final devices produced.

2.5.1   Optical Absorption Spectroscopy

OAS was used in this work for two main purposes: (i) assessing the concentration of graphene in the water-surfactant solution and (ii) determining the linear transmittance of the graphene film. A Perkin-Elmer Lambda 950 spectrometer with 1nm resolution is used for OAS. OAS can be used to estimate the concentration of graphene via the Beer-Lambert Law, according to the relation $A = \alpha c l$, where A is the absorbance, l is the light path length, c in g/l the concentration of dispersed graphitic material and α [l/(gm)] the absorption coefficient [28]. Figure 2.24 plots the OAS spectra of graphene dispersions obtained with some of the surfactants shown in Figure 2.20: the spectra are mostly featureless, as it is expected as a consequence of the linear dispersion of the Dirac electrons [9] [42]. Note also that the absorption increases in the UV region, as a signature of the van Hove singularity in the graphene Density of States (DOS) [32].
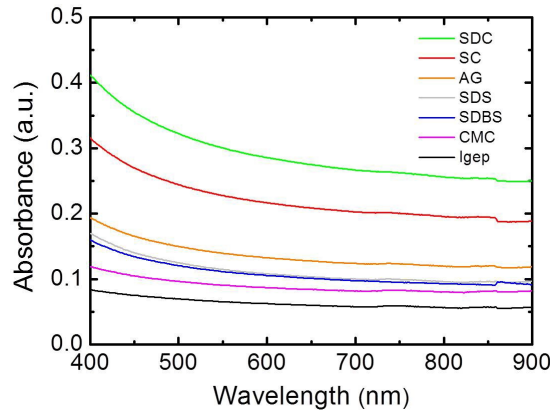
Figure 2.24: Optical absorption of graphene dispersed by bath ultrasonication in different water-surfactant solutions. Adapted from Ref. [58].

As already mentioned, the Beer-Lambert law is used to determine the concentration of the material, exploiting the absorption coefficient at 660nm equal to: $\alpha = 1390$ l/(gm) [36] [28]. Concentrations of about $0.18\,g/L$ in SDC-water solutions were reported by [27], while concentrations as high as 0.04g/l were reported by [16] (although this value is at least three times lower compared to other studies).

The same spectrometer can be used to determine the transmittance of a

graphene film, and provide a transmittance spectrum similar to that shown in Figure 2.15.

2.5.2   Raman spectroscopy of graphene

Raman spectroscopy is a fast, powerful and non-destructive characterisation method that makes use of inelastic light scattering to probe the vibrational properties of materials. This technique is particularly useful for organic materials in general, however it proves to be especially valuable for the carbon allotropes shown in Figure 2.9, including graphene [23]. The peculiar band structure of graphene further justifies the primacy of this characterisation technique: the absence of a bandgap makes all wavelengths of incident radiation resonant, thus the Raman spectrum contains information about both atomic structure and electronic properties [20]. Resonance could also be reached by ultraviolet excitation, either with the M-point Van Hove singularity or in the case of bandgap opening in chemically modified graphene [23] [20]. At the basis of the ability of Raman spectroscopy to probe modifications in the electronic properties of a material, (e.g. doping, defects, strain, disorder, chemical modifications, edges) there is the fact that Raman scattering on phonons is to a large extent determined by electrons: how they move, interfere and scatter. In this section I will describe the vibrational modes activated by Raman scattering in graphene, and the main features of the resulting Raman spectra [20].

Optical phonons in graphene:

Phonons are collective excitations in a periodic, elastic arrangement of atoms or molecules in condensed matter, i.e. vibrational energy units that arise from oscillating atoms within a crystalline or molecular structure [2]. Not all these vibrational modes are Raman active, i.e. not all these modes can be probed through Raman scattering. The Raman active modes in graphene are depicted in Figure 2.25, where E_{2g} is a doubly degenerate in-plane bond-stretching mode, and A_{1g} is the so-called *breathing mode* of the carbon hexagons, which is only activated by defects in the crystalline structure [20].
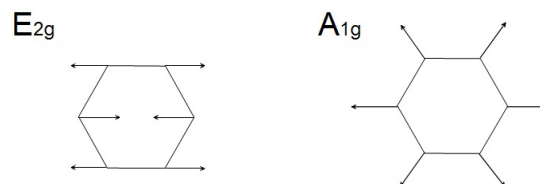
Figure 2.25: Active Raman modes in graphene.

In materials without an electronic band-gap, like graphene, the interaction of phonons with electrons must be considered when calculating phonon energies. In metals for example, the electronic screening of the atomic vibrations can occur in certain points of the FBZ. The consequent anomalous behaviour in the phonon dispersion relation, which it is determined by the shape of the Fermi surface, is called the *Kohn Anomaly* (KA), and appears as a kink in the phonon dispersion relation, i.e. a singularity in the dynamical matrix [2]. As already mentioned in section 2.3.2, the Fermi surface of graphene is limited to the two points K and K'. Thus, KA can occur only for phonons with $q = 0$ or q connecting the two Fermi points (i.e. $q = K$). KAs in graphene can be seen as sharp kinks for modes E_{2g} at Γ and A_{1g} at K, as depicted in Figure 2.26 [46].
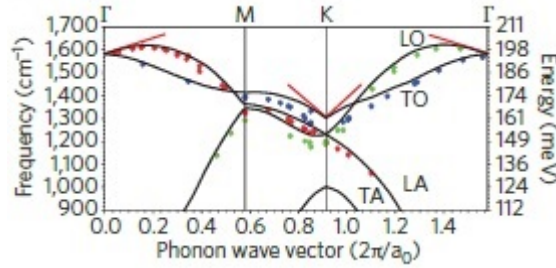
Figure 2.26: Dispersion relation for optical phonons: black curves represent the dispersion of in-plane phonon modes in graphene in the energy and frequency range relevant for Raman scattering. The red lines represent Kohn anomalies. Adapted from Ref. [20].

Figure 2.27 presents the Raman spectra of pristine and defected graphene, and it is now possible to explain the origin of the peaks.
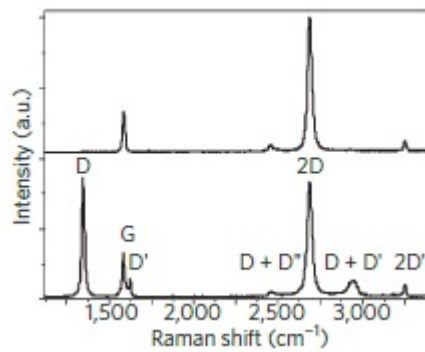
Figure 2.27: Raman spectra of pristine (**top**) and defected (**bottom**) graphene. Adapted from Ref. [20].

G peak:

The G peak set at a raman shift of approximately 1582cm^{-1} corresponds to the doubly-degenerate E_{2g} phonons at the FBZ centre Γ [22], and it is present both in pristine and defected graphene. The effects of doping on the graphene G-peak position (Pos(G)) and Full Width at Half Maximum (FWHM(G)) where reported in Ref. [15]. Pos(G) increases and FWHM(G) decreases for both electron and hole doping. The G peak stiffening is due to the non-adiabatic removal of Kohn-anomaly at Γ. The FWHM(G) sharpening is due to Pauli blocking of phonon decay into electron-hole pair, when the electron-hole gap is higher than the phonon energy and saturates for a Fermi shift bigger than half phonon energy [15]. By studying the G peak, it is also possible to assess the amount of disorder in the material: in pristine graphene, the position of the G peak does not depend on the excitation wavelength of the laser, but in disordered carbons Pos(G) increases as the excitation wavelength decreases, i.e. the G peak becomes dispersive [22].
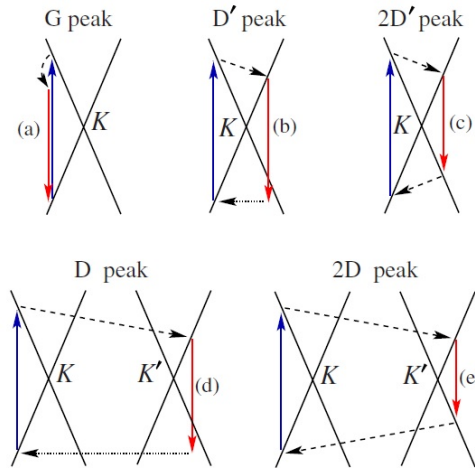
Figure 2.28: Role of the electron dispersion in Raman scattering: (a) intravalley one-phonon G peak, (b) defect-assisted intravalley one-phonon D' peak, (c) intravalley two-phonon 2D' peak, (d)defect-assisted intervalley one-phonon D peak, and (e) intervalley two-phonon 2D peak. Vertical solid arrows represent interband transitions accompanied by photon absorption (**blue lines**) or emission (**red lines**). Dashed arrows represent phonon emission. Horizontal dotted arrows represent defect scattering. Adapted from Ref. [5].

D, D', 2D and 2D' peaks:

The D peak is due to the breathing modes of sp^2 rings and requires a defect for its activation [46] [22]. It comes from TO phonons around the K point of the Brillouin zone, it is strongly dispersive with excitation energy due the KA

at K ($\approx 50\text{cm}^{-1}/\text{eV}$). The activation process for the D peak, called *Double Resonance* (DR)is shown schematically in Figure 2.28d: (i) a photon excites an electron/hole pair; (ii) electron-phonon scattering occurs with an exchanged momentum $q \approx K$; (iii) defect scattering; (iv) electron/hole recombination. The D peak intensity is not related to the number of graphene layers, but only to the amount of disorder [22]. DR can also happen as intra-valley process i.e. connecting two points belonging to the same cone around K (or K'), as shown in Figure 2.28b. This gives rise to the so-called D' peak, which can be seen around 1620cm^{-1} in defected graphene or close to the edges of the flake. The 2D peak is the second order of the D peak and it is a single peak in monolayer graphene, whereas it splits in four bands in bilayer graphene, reflecting the evolution of the band structure [21].
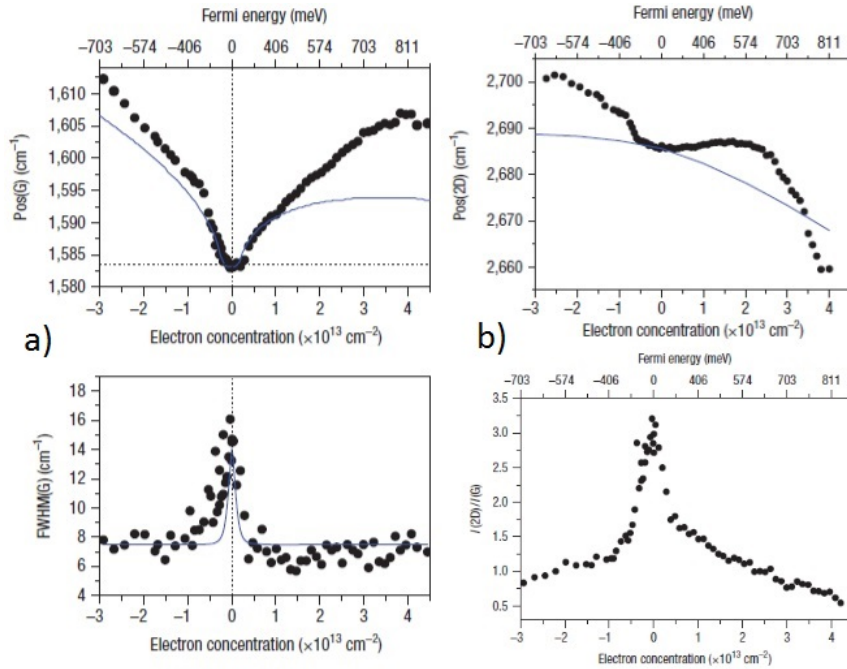
Figure 2.29: (a) Position of the G peak (**top**) and its FWHM (**bottom**) as a function of electron and hole doping. (b) Position of the 2D peak (**top**) and intensity ratio between the 2D and G peaks as a function of doping (**bottom**). The solid blue lines are theoretical predictions. Adapted from Ref. [15].

The 2D' peak is the second order of the D' peak. Since 2D and 2D' originate from a Raman scattering process where momentum conservation is obtained by the participation of two phonons with opposite wavevectors (q and $-q$), they do not require the presence of defects for their activation, and are thus always present. The 2D peak, as well as the G peak, can give quantitative information about the doping levels: the position of the 2D peak predicted to decrease for

an increasing electron concentration in the system. This allows the use of the 2D peak to discriminate between electron and hole doping (distinction that we are not able to do with the simple evaluation of the G peak); moreover, the ratio between the intensities of the 2D and the G peaks, i.e. I(2D)/I(G) can indicate the doping level [15].

2.5.3 Nonlinear optical transmittance

Different techniques can be used to study the optical nonlinearities associated with the change in refraction and absorption coefficients induced by intense laser power: in our work, I make use of a power-dependent transmission method to study saturable absorption. The material object of the study is exposed to a pulsed laser beam and, by means of a variable optical attenuator, the transmittance of the sample is detected and recorded at different power levels. Since the graphene films are not free-standing, i.e. they are deposited on top of a substrate (usually a quartz slide for this kind of measurements), the acquired data are normalised by the substrate transmittance. For an ideal Fast SA, which obeys equation 2.7, the curve showed in Figure 2.30 is obtained:
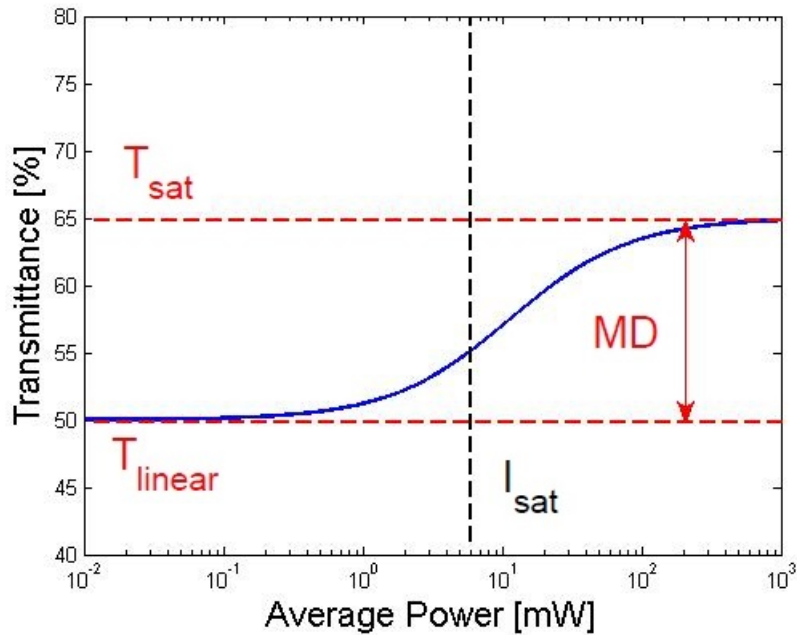
Figure 2.30: Simulation of the power-dependent transmittance of a generic fast SA, calculated using equation 2.7. T_{linear} is the linear transmittance of the SA, and I_{sat} the Saturation Intensity.

Two different setups where used to carry this measurement:

Nonlinear transmittance of graphene film on fibre connector

Graphene films transferred on top of fibre connectors were tested in the setup presented in Figure 2.31. In this system, as done in Ref. [50], the laser light is first coupled into an optical fibre and is thus conveyed into a variable optical attenuator. The output is then split in two lines: the first one goes directly into a power metre and acts as a monitor quantity, while the second passes through the SA sample and it is subject to nonlinear absorption. The intensity dependent transmittance is thus calculated as:

$$T = \frac{I_{sample}}{I_{monitor}} C_F \tag{2.35}$$

Where C_F is a calibration factor related to the splitting ratio of the two laser lines, which in our case is 70:30.
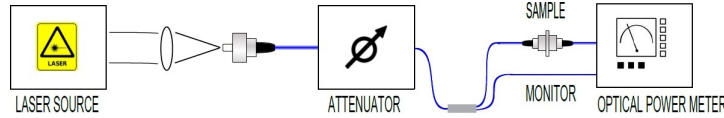
Figure 2.31: Setup for nonlinear transmittance measurements of graphene films transferred on fibre connectors.

The pulsed laser source typically is a mode-locked laser with sufficient pulse energy to saturate the SA under test. Ideally, the SA should be characterised under identical conditions as those found inside the laser cavity in which it operates. The pulsed laser source should therefore operate at the same center wavelength and pulse duration, and it should be able to provide the same or higher fluence. Our system was coupled to the output of a Coherent Chameleon Ti-Sapphire laser and Compact Optical Parametric Oscillator system, and the pulsed beam had the following characteristics: centre wavelength 1560nm, repetition rate 80MHz, pulse duration approximately 600fs. In later chapters (chapters 3 and 4) it will be shown that the value of repetition rate is approximately four times higher than that found in the laser cavity, and this will have to be considered when evaluating the nonlinear transmittance measurements.

Nonlinear transmittance of graphene film on quartz substrate

Graphene films transferred on quartz slides were tested in a different setup (see Figure 2.32), which is a transmittance-modified version of the setup proposed by Ref. [37].

The wide-dynamic range attenuator was obtained using polarization splitters in combination with polarization rotation optics; this method relies on two
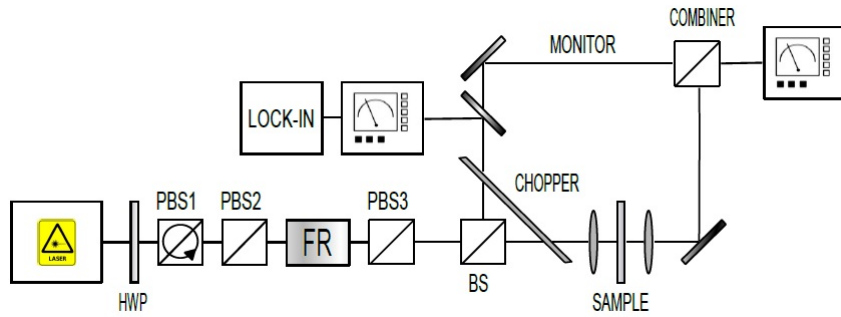
Figure 2.32: Setup for nonlinear transmittance measurements of graphene films transferred on quartzes.

optical elements: one element rotates the linear polarization state, whereas the second element selects the desired polarization (PBS1 and PBS2 in Figure 2.32). The angle of incidence onto the SA is perpendicular, and hence some light is reflected back into the laser source. An isolator prevents such back-reflections from entering the laser source, which would lead to mode-locking instabilities. The isolator consists of two polarizing beam splitters PBS2 and PBS3 and a Faraday rotator. The measurement part consists of a non-polarizing beam splitter cube (BS), a chopper wheel and a photo detector (PD). Instead of detecting the monitor and the sample signals simultaneously by two different detectors, they are separated in time and measured with the same detector system. The separation in time is achieved by a chopper wheel which is able to simultaneously chop both arms and it is put close to the 50:50 beam splitter. The signal is amplified with a variable current amplifier and measured with an analog-to-digital (AD) converter and recorded with a computer. The chopper frequency is typically around 100s of Hertz. The chopper wheel is lifted such that the axis of the chopper wheel is a few millimetres above the beam. During one chopper wheel cycle, four different states occur: (i) only the reference beam is measured, (ii) both beams measured, (iii) only the sample beam is measured, and (iv) both beams are blocked. The signal in the fourth phase corresponds to a background signal from photodiode dark current and environmental background light, which is then subtracted from the measurement signal in the first and third phases. The transmittance value is then obtained by dividing the intensities in phase (iii) and phase (iv).

The centre wavelength was 960nm instead of 1560nm and the repetition rate 80MHz rather than 20MHz; the beam spot-size on the sample and the pulse duration was comparable with the values obtained in the laser cavity (See chapter 4), that is 7.8 μm (beam waist, $1/e^2$ radius) and 200fs respectively.

Chapter 3

Graphene SA preparation

This Chapter will give a detailed description of the preparation of graphene SAs, both graphene films and graphene-PVA composites. It will also present the results of the material characterisation, which include optical, spectroscopic and morphologic studies.

3.1 Graphene dispersion preparation and characterisation

The graphene dispersion preparation follows the procedure explained in section 2.4.1. Graphite flakes (380mg, Sigma Aldrich) where mixed in a water-surfactant solution (240mg $\div$ 40 ml) and exposed to a mild ultrasonication bath in a Branson 450A ultrasonicator for approximately 9 hours at 10°C.
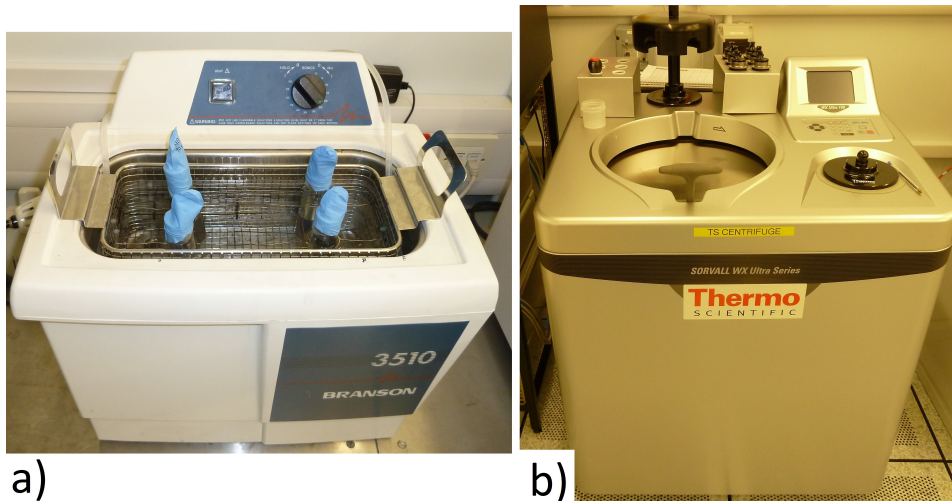
Figure 3.1: Branson 450A (25W) bath Ultrasonicator (a) and Sorvall WX-100 Ultracentrifuge (b).

Surfactant	Absorbance [a.u]	Dilution Ratio	Concentration [g/l]
SDC	1.05747	10:1	0.084
SC	0.29721	1:10	0.235

Table 3.1: Graphene dispersions in water-surfactant solutions.

The surfactants chosen for stabilizing the dispersion were SC and SDC. As explained in section 2.4.2, these amphiphilic molecules show a relatively large hydrophobic contact area per molecule ($1.8 - 3\text{nm}^2$) which leads to a better adsorption to the graphitic planes than other surfactants. After sonication, ultracentrifugation in a Sorvall WX-100 Ultracentrifuge was carried on the dispersion for 1 hour at 10krpm. Thanks to the sedimentation process, the thicker graphitic flakes are separated from the SLG (or FLG) dispersion along with the unexfoliated material. The top 70% of the dispersion is then collected and characterised.

3.1.1   Optical Absorption Spectroscopy

Figure 3.2 shows the absorption spectrum of the graphene dispersion diluted in the water-surfactant solution. Apart for the peak at approximately 270nm due to the Van Hove singularity in the DOS, the spectrum is featureless thanks to the broadband absorption of graphene [32] [42]. From this spectrum it is possible to determine the concentration of material dispersed by applying the Beer-Lambert law, as shown in section 2.5.1; by using an absorption coefficient at 660nm equal to $\alpha = 1390 \, \text{l/(gm)}$ I obtained the values reported in Table 3.1 [28] [36]:
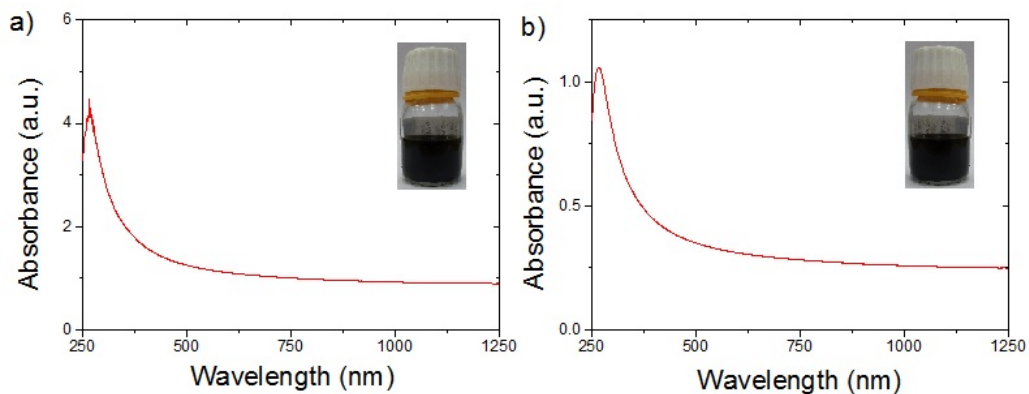
Figure 3.2: Absorption spectra of the two dispersion prepared: a) graphene in SDC-water solution (the ratio between the dispersion and the reference solution is 10:1) and b) graphene in SC-water solution (the ratio between the dispersion and the reference solution is in this case 1:10). In both the spectra, the reference solution optical absorption has been subtracted. Insets: undiluted dispersions.

The concentrations reported in Table 3.1 are not consistent with what has been reported in literature by Ref. [27]. The graphene dispersion in SDC-water solution shows a concentration value which is less than half the one reported by [27] (0.18g/l). For this reason I decided to employ only the graphene dispersion in SC-water solution for the graphene films production.

3.1.2 Multi-wavelength Raman Spectroscopy

In order to characterise the graphene dispersion, prepared as shown in the previous paragraphs, I drop-cast a few hundred of microlitres of dispersion on a Si/SiO_2 substrate positioned on a hot-plate (90^oC) to evaporate the water. Figure 3.3 presents four dark-field optical images of the drop-cast dispersion, taken with different objectives.
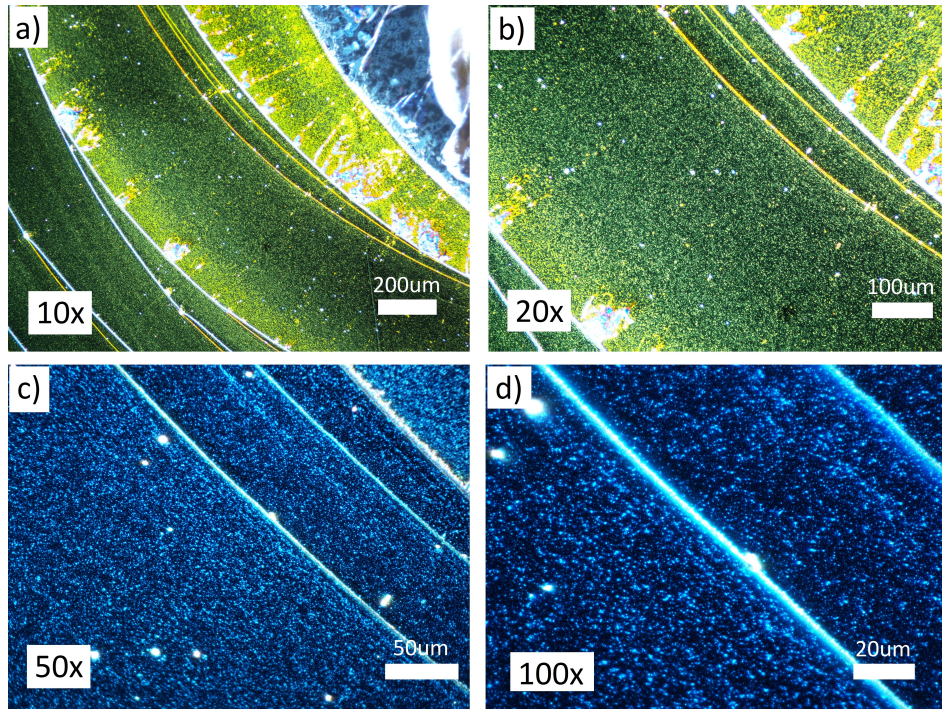
Figure 3.3: Dark-field optical images of graphene dispersion drop-cast on Si/SiO_2.

Raman spectra of the drop-cast dispersion were taken with a Renishaw InVia micro-Raman spectrometer at three different laser wavelength: 633nm, 514.5nm and 457nm. For each wavelength, up to twenty points were taken in order to obtain a wide data set to be analysed statistically. Figures 3.6a, 3.7a and 3.8a plot the typical Raman spectrum of the Graphene Dispersion drop-cast on Si/SiO2.

Firstly, it is important to note that the 2D-peak, fits with less than 0.1%

error with a single Lorentzian function: this feature is indeed a single band in SLG, whereas it splits in four in BLG, reflecting the evolution of the band structure [21]. As mentioned in section 2.4.1, at the end of the exfoliation process, the dispersion contains a variety of graphitic material, ranging from SLGs and FLGs to bulky graphite flakes. While the latter are removed through centrifugation, FLGs and BLGs still coexist in the dispersion together with the SLGs. However, the presence of single 2D peak rather than a wide band, as presented in Figures 3.6a, 3.7a and 3.8a, tells us that the graphene layers in the dispersion are electronically decoupled, and hence they all behave as SLGs [21].

The second important point regards the presence of strong D and D' peaks which, unlike the 2D and 2D', are activated by defects through DR. The D and D' peaks are assigned to the edges of the submicrometer graphene flakes, rather than to the presence of a large amount of disorder within the flakes. This is further supported by the low Disp(G), as shown in Figure 3.4, which plots Pos(G) for each laser wavelength: a linear fit of the data assesses the dispersion of the G peak to be approximately $0.04 \text{cm}^{-1}/\text{nm}$, which corresponds to a defect content in terms of sp^3 bonds equal to 0% [19].
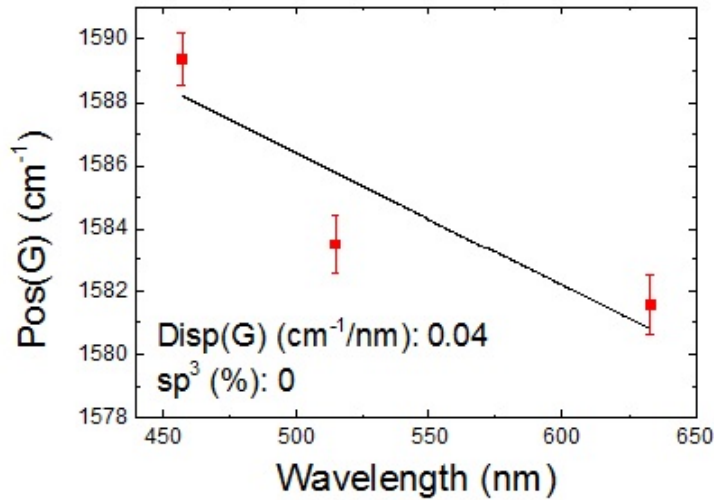
Figure 3.4: G peak position for each laser wavelength.

The full width at half-maximum of the G peak, FWHM(G), always increases with disorder. Thus, combining the intensity ratio of the D and G peaks, I(D)/I(G), with FWHM(G) allows us to discriminate between disorder localized at the edges and disorder in the bulk of the samples. In the latter case, a higher I(D)/I(G) would correspond to higher FWHM(G). Figures 3.6g, 3.7g and 3.8g show that I(D)/I(G) and FWHM(G) are not correlated, a clear indication

that the major contribution to the D peak comes from the sample edges.
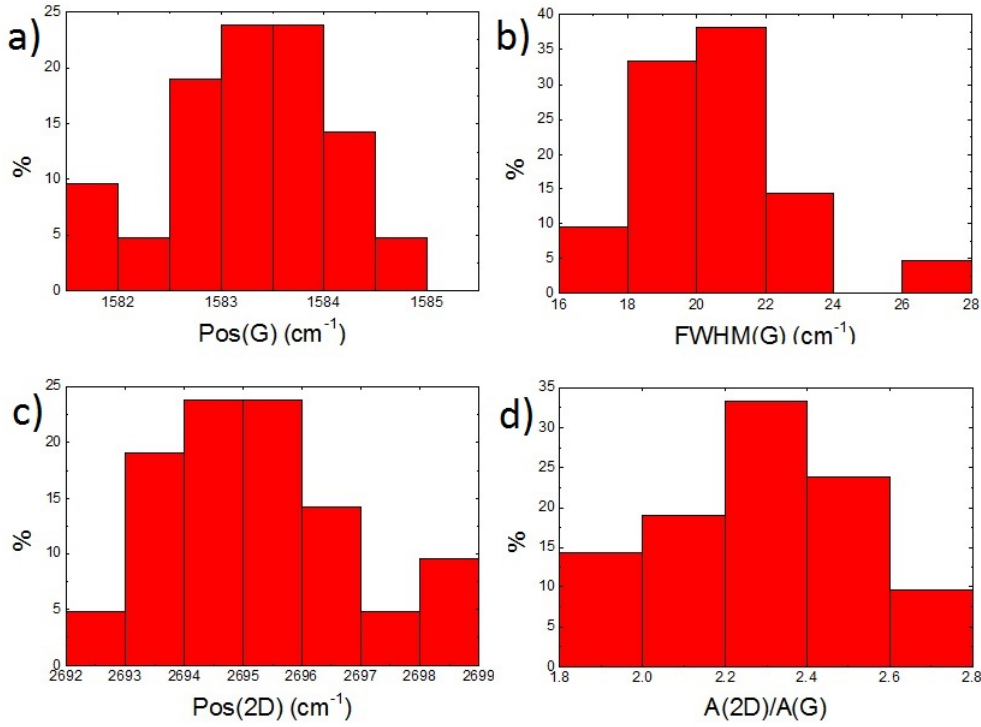
Figure 3.5: Doping analysis carried at 514.5nm.

The doping analysis was carried by considering the statistical distribution of the following quantities: Pos(G), FWHM(G), Pos(2D) and A(2D)/A(G) at 514.5nm. Figure 3.5a shows that Pos(G) is around $1583 - 1584\text{cm}^{-1}$, while FWHM(G) is around 21cm^{-1} (Figure 3.5b). This corresponds to a charge carrier concentration of less than $0.5 \times 10^{13}\text{cm}^{-2}$, e.g. very intrinsic graphene, almost undoped [15]. Figures 3.5c and 3.5d also show that Pos(2D) is around 2695cm^{-1} and that the area ratio A(2D)/A(G) is at most 2.8, which corresponds to a Fermi level set at approximately 0.338eV.

In Figures 3.6, 3.7 and 3.8, the results of the statistics carried on the Raman spectra are presented for each laser wavelength.
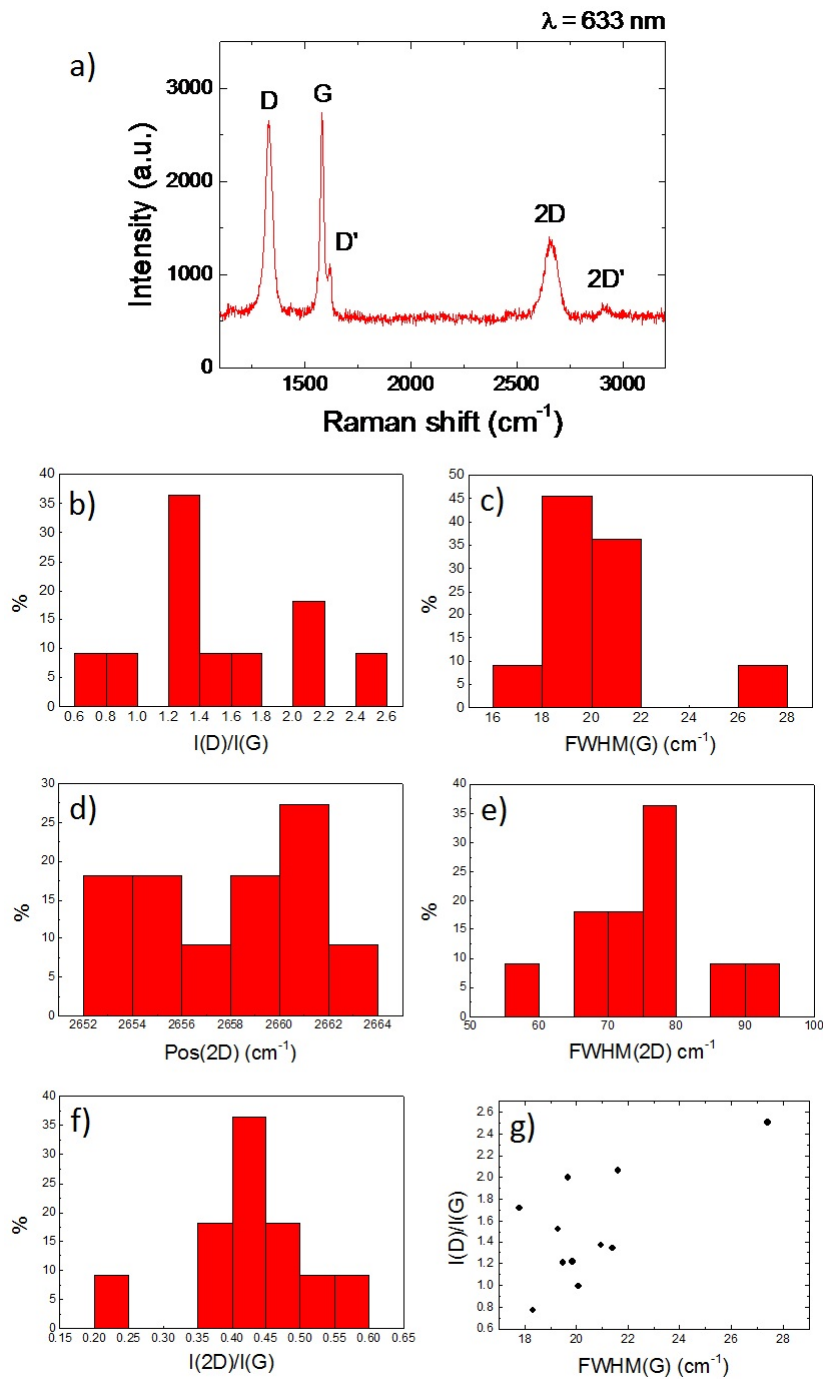
Figure 3.6: (a) Raman spectrum of graphene dispersion deposited on Si/SiO2 at 633nm. Distribution of (b) I(D)/I(G), (c) FWHM(G), (d) Pos(2D), (e) FWHM(2D), (f) I(2D)/I(G), and (g) I(D)/I(G) as a function of FWHM(G) for 11 measurements.
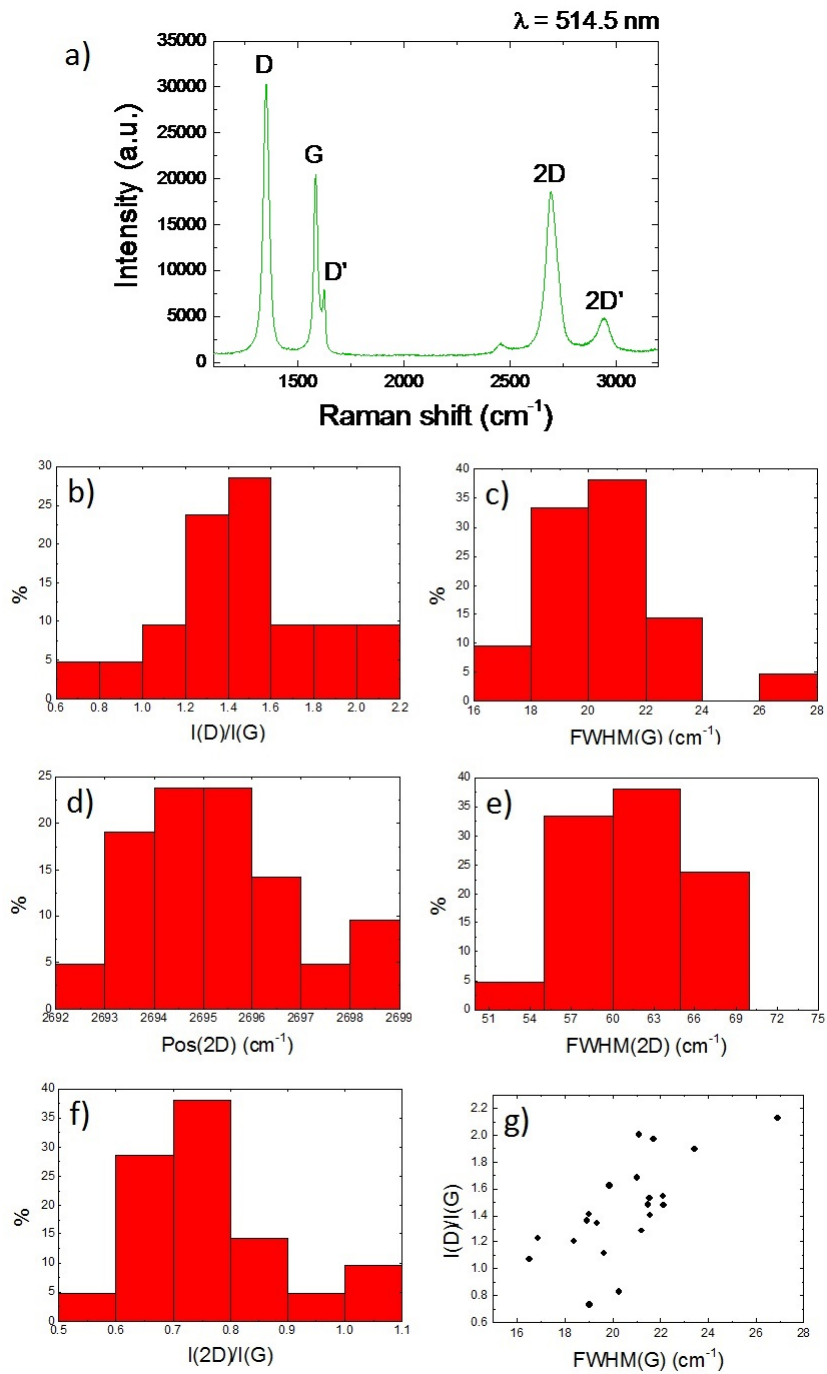
Figure 3.7: (a) Raman spectrum of graphene dispersion deposited on Si/SiO2 at 514.5nm. Distribution of (b) I(D)/I(G), (c) FWHM(G), (d) Pos(2D), (e) FWHM(2D), (f) I(2D)/I(G), and (g) I(D)/I(G) as a function of FWHM(G) for 21 measurements.
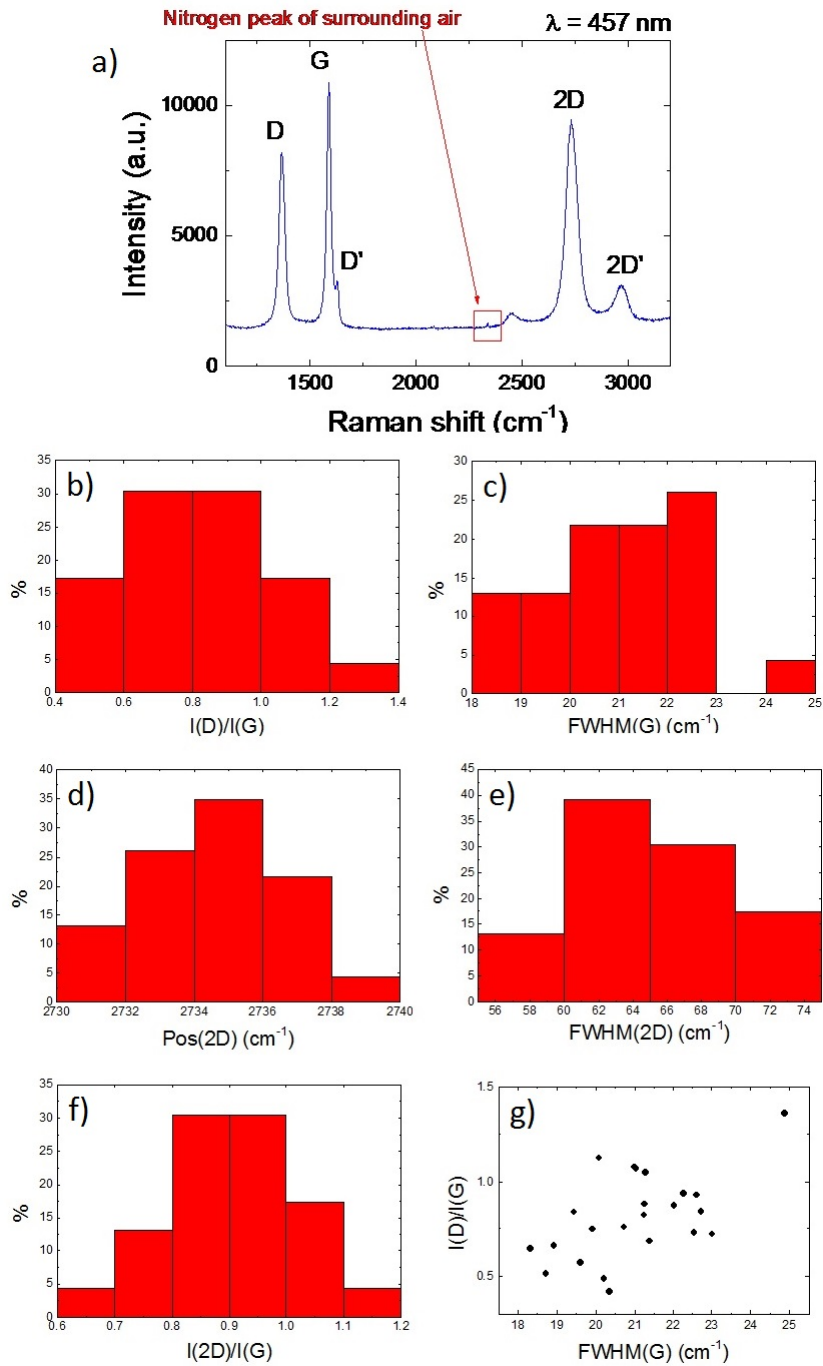
Figure 3.8: (a) Raman spectrum of graphene dispersion deposited on Si/SiO2 at 457nm. Distribution of (b) I(D)/I(G), (c) FWHM(G), (d) Pos(2D), (e) FWHM(2D), (f) I(2D)/I(G), and (g) I(D)/I(G) as a function of FWHM(G) for 23 measurements.

3.2 Graphene film preparation and transfer on fibre connectors

In the previous section, the graphene dispersion preparation process was presented. I will now describe how graphene films are produced and transferred on the fibre connectors.

3.2.1 Graphene film preparation by vacuum filtration

Figure 3.9 shows two images of the setup utilised for the vacuum filtration:
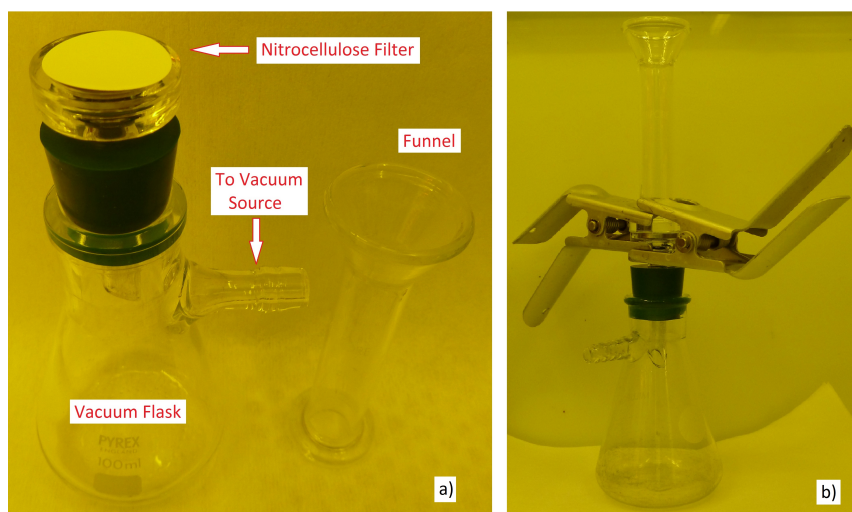
Figure 3.9: Setup for vacuum filtration: (a) components and (b) assembled.

Once the setup is assembled (Figure 3.9), the filtration consists of two steps: (i) the funnel is loaded with a precise volume of graphene dispersion (usually few hundreds of microlitres), and vacuum is generated in the vacuum flask by using a rotative pump connected to the dedicated outlet. The dispersion is thus filtered through a Nitrocellulose filter (Millipore, 100nm pore-size), separating the graphene flakes, which are blocked by the filter, from the water-surfactant solution, which flows into the vacuum flask. (ii) Once the dispersion has been completely filtered, the funnel is again loaded with approximately 15ml of deionized water while the vacuum pump is still running: this step is carried in order to wash away the surfactant molecules that may be trapped among the graphene flakes. Figure 3.10 shows a picture of two Nitrocellulose filters before and after graphene has been deposited through vacuum filtration. The dark portion of the filter, as it can be seen in Figure 3.10, is the graphene film that can thus be transferred on other substrates.
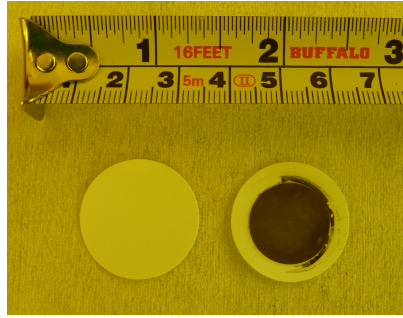
Figure 3.10: Millipore 100nm pore-size Nitrocellulose filters, before and after vacuum filtration of a graphene dispersion.

3.2.2   Graphene film transfer on fibre connector

Figure 3.11 shows the steps of the original transfer process that was devised in order to integrate the graphene film, produced as explained in the previous section, in the laser cavity. (i) A piece of graphene film on the nitrocellulose filter of approximately few square millimiters is cut with a scalpel, dipped in de-ionised water and placed on the tip of a fibre connector. The wetting removes the majority of the air bubbles trapped in the film and facilitates the positioning of the small piece of film on top of the likewise small tip of the fibre connector. (ii) The position of the film is fixed with some clippers and a piece of glass slide. The system is then placed at a temperature of approximately 90ºC for 1 hour. The pressure applied and the heat improve the adhesion of the film to the fibre connector. (iii) After the pressure and heat treatment, the glass slide and the clippers are removed and the fibre connector is placed in acetone for approximately 60 hours. The solvent dissolves the Nitrocellulose filter to which the graphene film is still attached. (iv) The last step consists of a IPA-water bath to further clean the exposed surface of the graphene film.
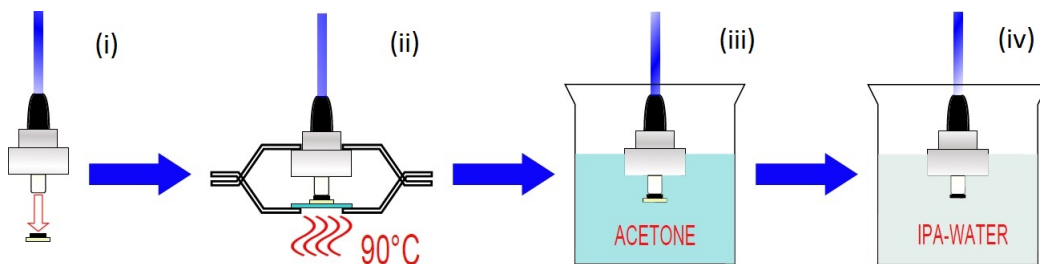
Figure 3.11: Schematics of the graphene film transfer process on the fibre connector tip.

The result of the transfer process can bee seen in Figures 3.12 and 3.13.
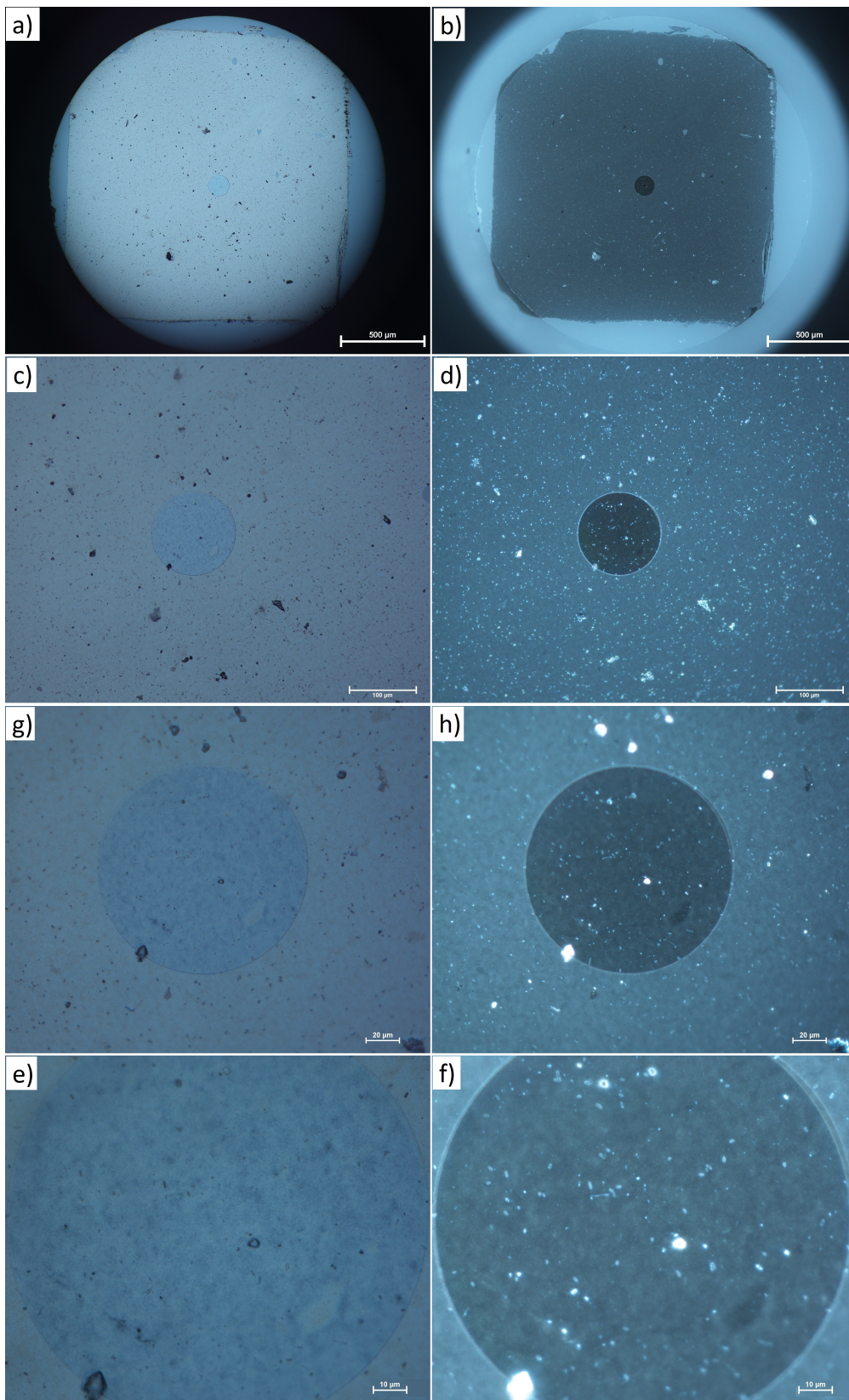
Figure 3.12: Microscope images of graphene film transferred on fibre connector: 5x (a) and (b), 20x (c) and (d), 50x (e) and (f), 100x (g) and (h). On the **left** are the bright field images, while on the **right** the dark field ones.

Figure 3.13: Graphene film transfer on fibre connector.

3.2.3   Graphene film thickness and linear transmittance

In order to fully characterise the produced graphene films, portions of them were transferred on quartz slides following a procedure similar to the one presented in Figure 3.11. The optical transmittance spectrum was taken for each film with the Perkin-Elmer Lambda 950 spectrometer (Figure 3.14), whilst the thicknesses were evaluated with a Bruker DekTak XT profilometer. In Table 3.2 are the values for the linear transmittance at 1550nm (operation wavelength of the laser used) and thickness for different graphene films, i.e. for films produced starting with different volumes of the same dispersion (graphene in SC-water solution, graphitic material concentration: 0.235g/l).
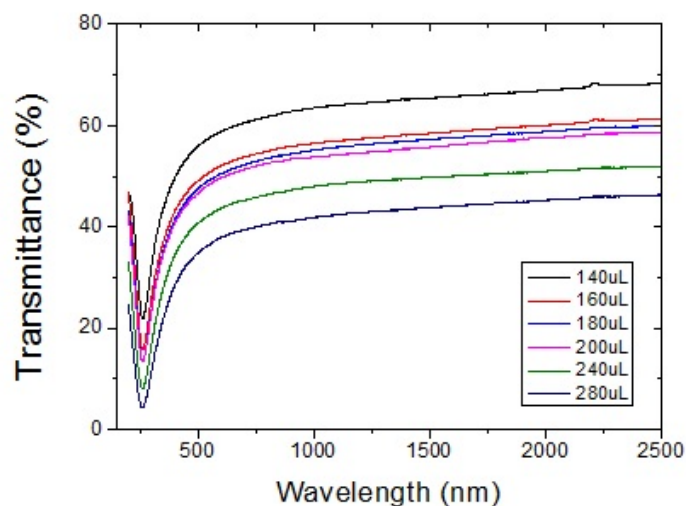
Figure 3.14: Optical transmittance spectra of different graphene films.

Volume [μl]	Average Thickness ($\pm\sigma$) [nm]	Transmittance (at 1550)nm [%]
140	28 ± 5	65.6
160	39 ± 9	58.6
180	57 ± 8	57.4
200	47 ± 10	55.9
240	65 ± 20	49.9
280	76 ± 18	43.9

Table 3.2: Graphene films prepared with different volumes of of the same dispersion.

From Figure 3.15, which is a graphic representation of Table 3.2, it can be seen that both the transmittance and the average thickness depend linearly on the volume of dispersion used, as it is reasonable to expect if it is assumed that the vacuum filtration process scales linearly with the amount of material employed. The thickness measurements show a standard deviation that increases with the average thickness of the material, while the transmittance values did not show significant deviations.
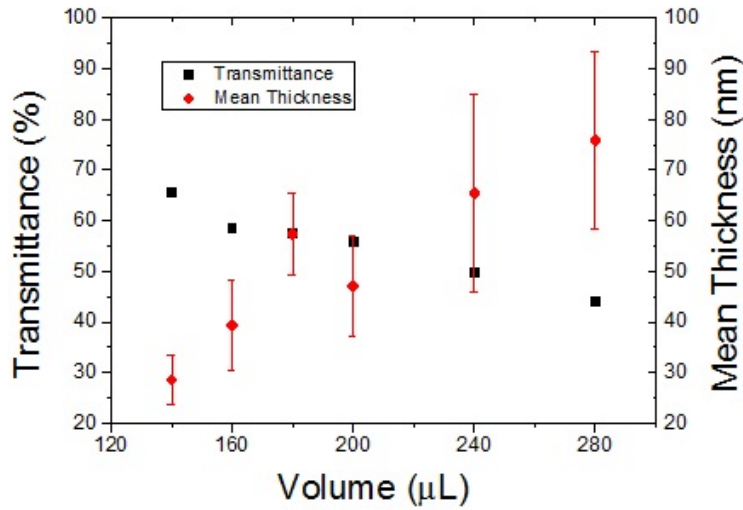
Figure 3.15: Relation between volume of graphene dispersion used to produce the films, and their relative transmittance and thickness.

This behaviour may be due to the fact that the films' profiles had to be sampled from the edges of the films, which can be less homogeneous. Another possible explanation is that the entire films become less homogeneous with increasing volume of material, but only the thickness measurements are affected since the spot-size of the light beam in the spectrometer is of the order of few square millimetres, and thus a inherent averaging mechanism is carried on the transmittance values. The nonlinear optical trasmittance measurement pre-

sented later in this work, which employed a laser beam with a much smaller spot-size, approximately few tens of square micrometers, showed a quite good homogeneity of the films in terms of transmittance. This consideration seems to suggest that the high values of standard deviation for the thick films are due to border effects rather than being an indication of a general inhomogeneity of the films, however a proper investigation on this issue should be undertaken.

3.2.4   Raman Spectrum of graphene film on fibre connector

In order to fully verify the success of the transfer technique presented in section 3.2.2, Raman spectroscopy was carried on the graphene films transferred on the tip of the fibre connector. Figure 3.16 presents the comparison of two Raman spectra (laser wavelength: 514.5nm)taken from the graphene dispersion and the graphene film. Apart from minor differences, both of the spectra present similar features (Pos(G), FWHM(G), Pos(2D), I(D)/I(G)), thus confirming the success of the transfer process.
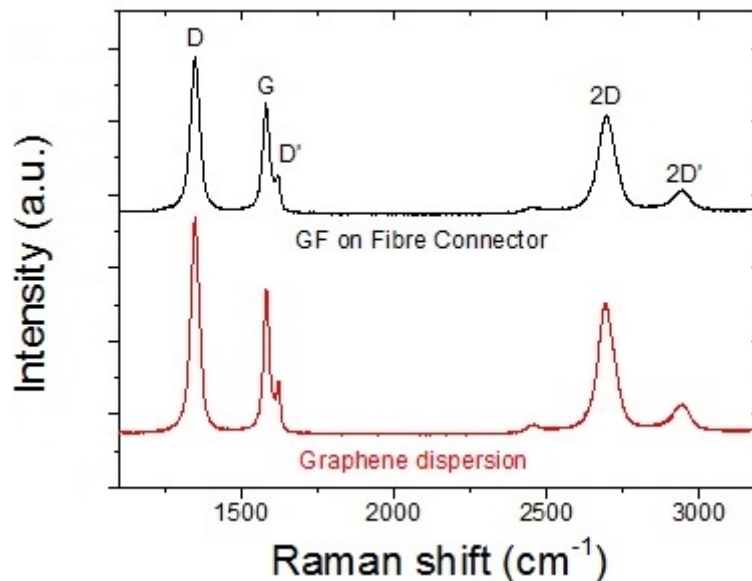
Figure 3.16: Comparison of Raman spectra taken on the drop-cast graphene dispersion and on the graphene film transferred on the tip of the fibre connector.

3.3   Graphene-PVA composite production

Graphene-PVA (Polyvinyl Alcohol) composites were also prepared according to Ref. [27]. The graphene-PVA composite is prepared by mixing 4ml of the centrifuged graphene dispersion with 120mg of PVA (Polyvinyl Alcohol) in ac-

queous solution in a speedmixer for 5 min at 3 krpm. The mixture is then evaporated at 20^oC, resulting in an approximately 50 μ m thick composite. Figure 3.17 shows an image of the composite, while in Figure 3.18 the transmission spectra of both the graphene-PVA and the PVA alone polymer are presented.
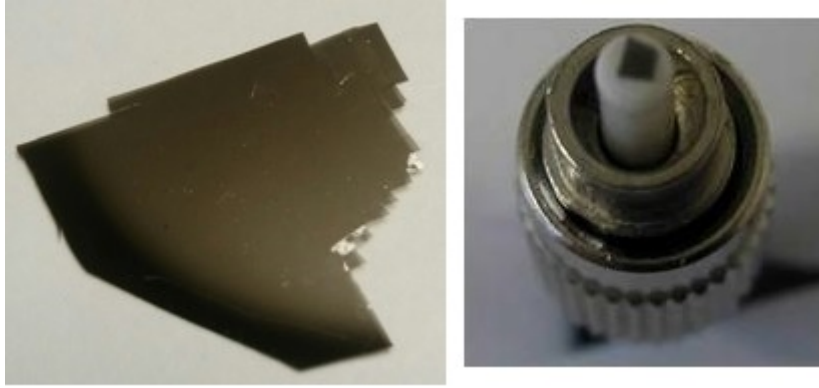
Figure 3.17: Photograph of a piece of graphene-PVA composite (**left**) and of smaller piece placed on the tip of a fibre connector (**right**).
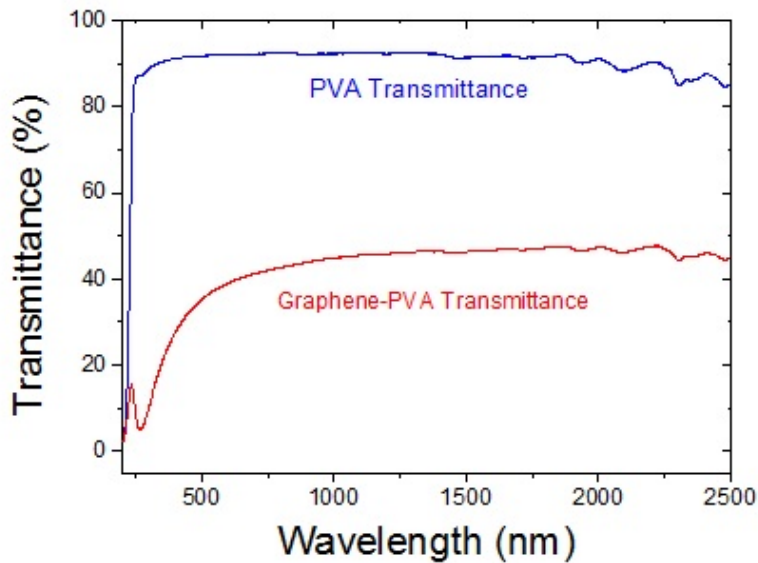
Figure 3.18: Transmittance spectrum of graphene-PVA composite.

3.4   Graphene SA characterisation

The graphene SAs nonlinear absorption and optical stability was characterised using the setups described in section 2.5.3.

3.4.1 Non-linear optical transmittance of graphene film on fibre connector

The graphene films transferred on the fibre connectors were tested in the setup depicted in Figure 2.31. The results of the characterisation are shown in Figures 3.19, 3.20 and 3.21 for graphene films of different thickness. It can be seen that all the samples show a definite intensity-dependent behaviour; however all the curves differ from that presented in Figure 2.30 as they do not reach a plateau at high intensities. Indeed, the maximum incident average power that could be coupled on the samples was approximately 25mW: this limitation was due mainly to the inherent losses of the coupling system and of the variable attenuator, as well as some non-linear effects that were affecting negatively the laser pulse shape (e.g. pulse splitting) above that power level. For this reason, the data here presented do not allow a complete assessment of the relevant parameter of the Fast SA, i.e. MD and Saturation Intensity, although it is still possible to evaluate the non-linear behaviour of the devices in the operating laser cavity, as done by Ref. [53] with lower available incident average power.
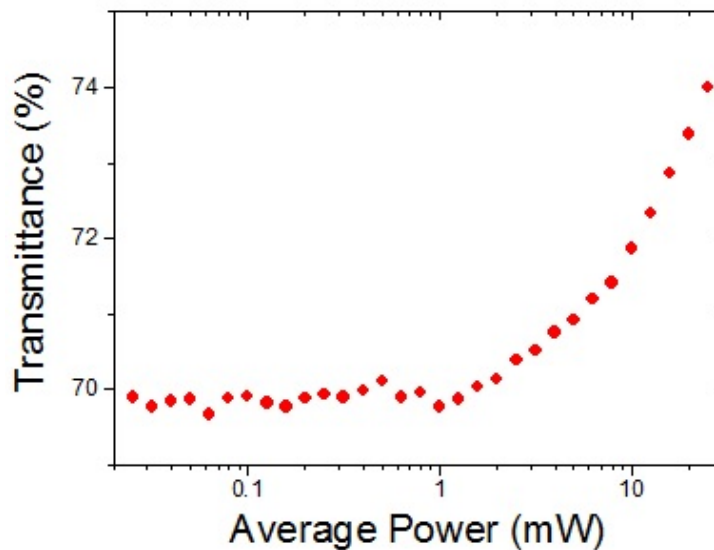
Figure 3.19: Nonlinear transmittance measurements of graphene film produced with 140 μl of graphene dispersion. The modulation of the transmittance is approximately 4.5% when increasing the incident power up to 25 mW.
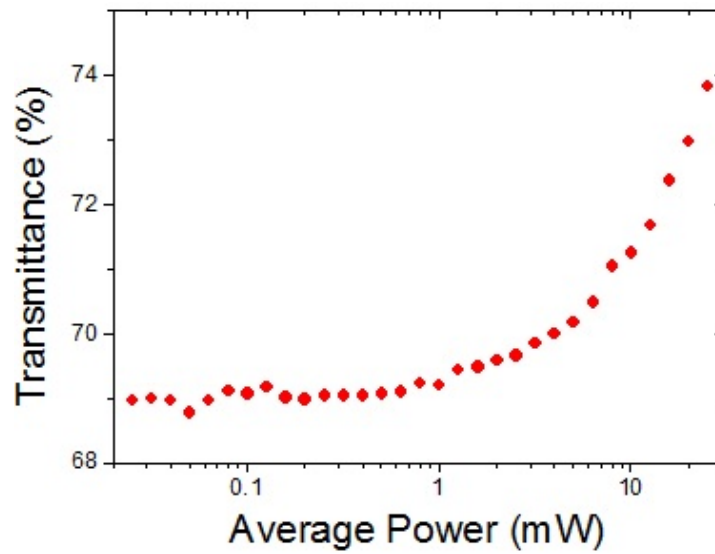
Figure 3.20: Nonlinear transmittance measurements of graphene film produced with 160 μl of graphene dispersion. The modulation of the transmittance is approximately 4.8% when increasing the incident power up to 25 mW.
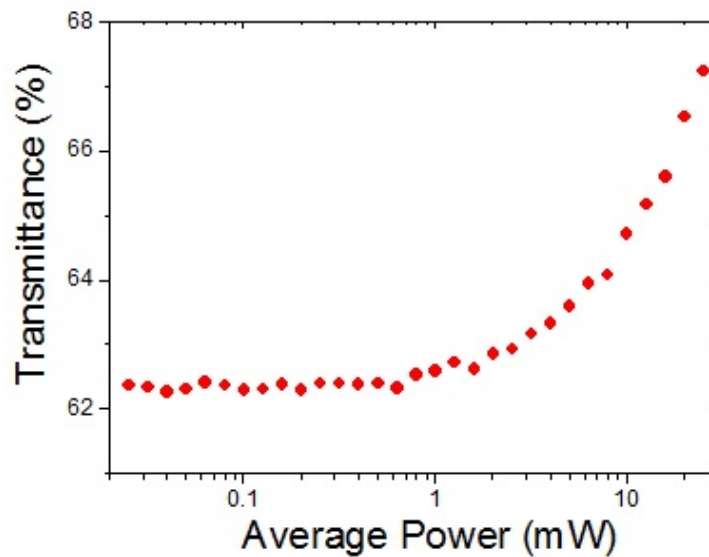
Figure 3.21: Nonlinear transmittance measurements of graphene film produced with 180 μl of graphene dispersion. The modulation of the transmittance is approximately 5% when increasing the incident power up to 25 mW.

3.4.2   Optical damage: a comparison between graphene film and Graphene-PVA

In several previous works, graphene-PVA composites have successfully been used as SA in fibre lasers to produce ultrafast pulses [53] [26] [47]. However, the continuous effort towards shorter pulse duration, higher repetition rate and power level did raise some questions regarding the optical stability of the SA. In particular, the main concern regarded the polymer matrix hosting the graphene flakes, i.e. the active material, which in principle could be more sensitive to both thermal and non-thermal optical damages. In this section, I present some evidence of the fact that the graphene films are indeed less subject to optical degradation than graphene-PVA composites.

Measurements carried in the fibre-setup

The first test consisted in carrying the nonlinear absorption measurement on a piece of graphene-PVA composite, sandwiched between two fibre connectors (Figure 2.31 in the same way it is usually placed into the laser cavity. This measurements were also carried by [53] in a similar setup, with two important differences: (i) the maximum power level was approximately 6mW (a factor of four lower than the setup used in this work), and (ii) the repetition frequency was 38.83MHz against the 80MHz of our setup. I attribute the different results obtained to these discrepancies :

- the higher available power ideally allows us to access the behaviour of the SA at higher saturation regimes, as already mentioned in section 3.4.1, and thus potentially obtain a higher value of transmittance modulation;

- the higher repetition rate for the same pulse energy implies a higher incident average power, and thus it is reasonable to expect a higher local temperature on the sample. This aspect is relevant if we consider that Reference [53] measures a modulation in transmittance of approximately 1.3% due to saturable absorption, whilst in our measurements this modulation it is hidden by the onset of a damage mechanism, probably related to both thermal and non-thermal effects. Hence, I attribute the absence of evident saturable absorption in our graphene-PVA samples to the onset of a damage mechanism enhanced by the high repetition frequency, although it is clear that further investigations are needed in order to clarify this point.

Figure 3.22 shows the results of the nonlinear transmittance measurement carried on a piece of graphene-PVA composite. The first thing that can be

noticed is the dramatic drop in transmittance, visible starting at approximately 5mW, which I attribute to a damage of the SA:
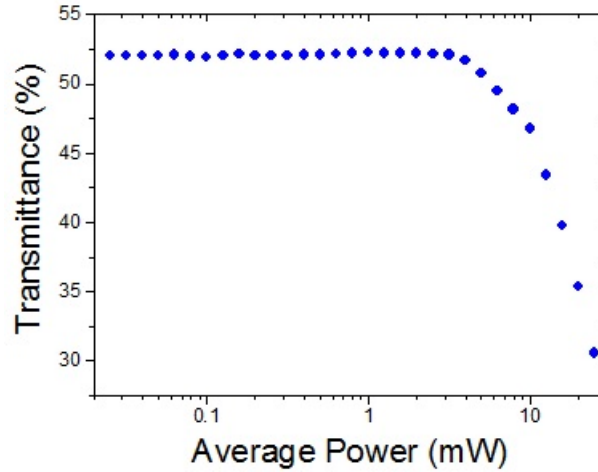
Figure 3.22: Nonlinear transmittance measurement of a piece of graphene-PVA composite.

Consecutive measurements carried on the same sample (Figure 3.23) seem to indicate than the damages are partially recovered, for the low transmittance values are similar at each iteration of the measurement.
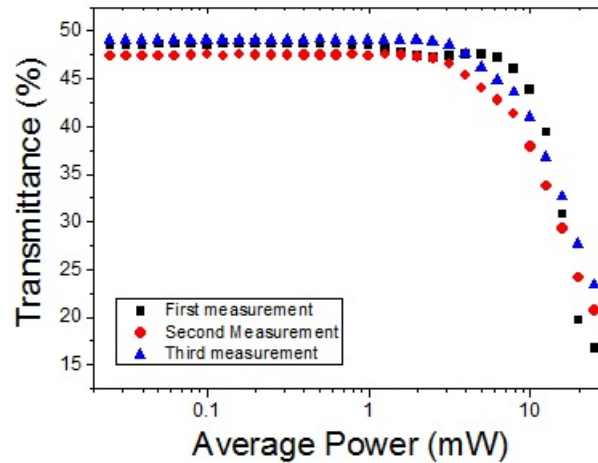
Figure 3.23: Three consecutive nonlinear transmittance measurements carried on the graphene-PVA sample: the dramatic drop in transmittance is an indication of degradation. The close resemblance of the three curves suggest a sort of recovery mechanism of the polymer matrix.

In order to verify whether a protracted exposure to the pulsed laser beam would permanently damage the composite, the sample was exposed at three different power levels for 10 minutes each; a nonlinear transmittance measurement was then carried at the end of each time interval. The data plotted in Figure

3.24 show how the composite material undergoes a progressive alteration of its optical properties, i.e. it is subject to a decrease in transmittance.
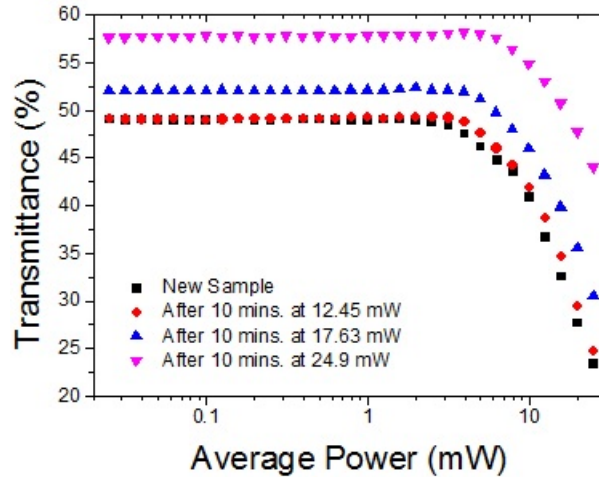
Figure 3.24: Nonlinear transmittance measurement on a piece of graphene-PVA composite exposed for 10 minutes to a pulsed laser at three different power levels: in **red** 12.45mW (−3dB), in **blue** 17.63mW (−1.5dB) and in **pink** 24.9mW (0dB).

These results can be compared to what obtained on graphene films transferred on a fibre connector, subject to the same experiment:
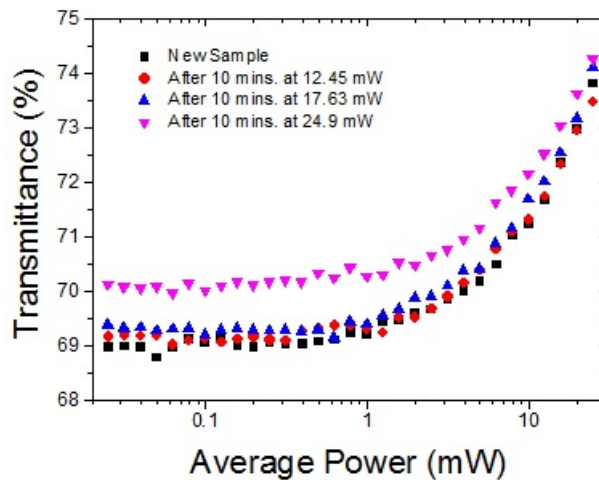
Figure 3.25: Nonlinear transmittance measurement on a graphene film transferred on top of a fibre connector exposed for 10 minutes to a pulsed laser at three different power levels: in **red** 12.45mW (−3dB), in **blue** 17.63mW (−1.5dB) and in **pink** 24.9mW (0dB).

The graphene film transmittance changes slightly (approximately 1%) only after being exposed to the highest power level for 10 minutes, thus showing a definite advantage with respect to the graphene-PVA composite in terms of stability in high-power conditions.

Measurements carried in the open setup

The second set of experiments devised to evaluate the optical stability of the graphene SAs, made use of the setup shown in Figure 2.32. It should be stressed again that, as already mentioned in section 2.5.3, measurements were performed at 960nm rather than 1560nm. The tests were carried on a graphene film transferred on a quartz slide and then sandwiched with another quartz slide, as shown in Figure 3.26, in order to simulate the pressure applied by the fibre connectors in the real cavity. All the transmittance data presented here were divided by the reference sample transmittance, i.e. two quartz samples.
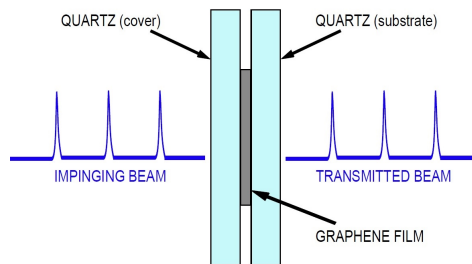
Figure 3.26: Graphene film sandwiched between two quartz slides in order to simulate the pressure applied by the fibre connectors in the real cavity.

In Figure 3.27 a standard measurement of nonlinear transmittance is presented. In this case the maximum power applied is approximately 30 mW: above this value I witnessed a degradation of the graphene film during the measurement. In the next four Figures the change in transmittance with time is shown for a period of approximately 10 minutes, using the same setup.
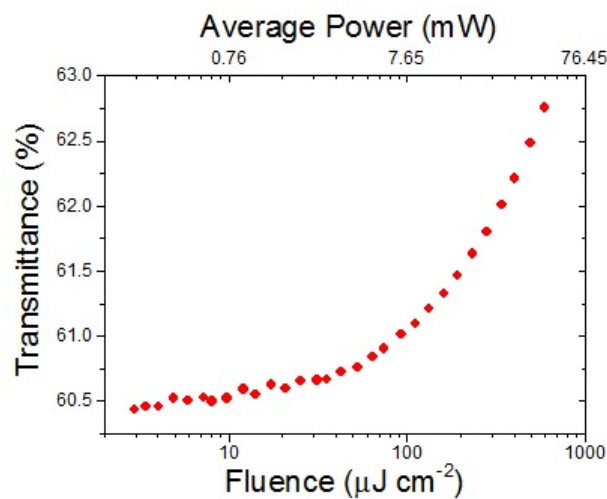
Figure 3.27: Graphene film sandwiched between two quartz slides in order to simulate the pressure applied by the fibre connectors in the real cavity.
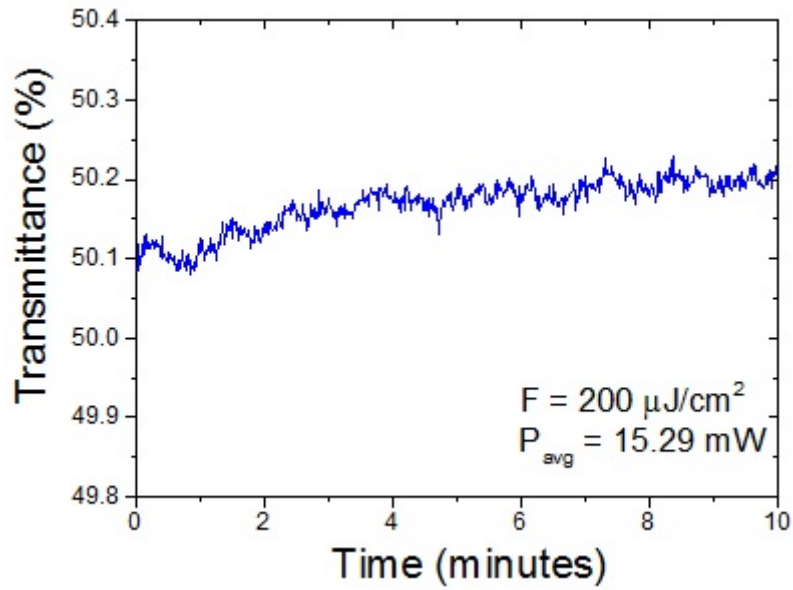
Figure 3.28: Change in transmittance with time of graphene film sandwiched between two quartz slides, exposed to a pulsed laser at an average power of 9.73mW $(200\mu J/cm^2)$.
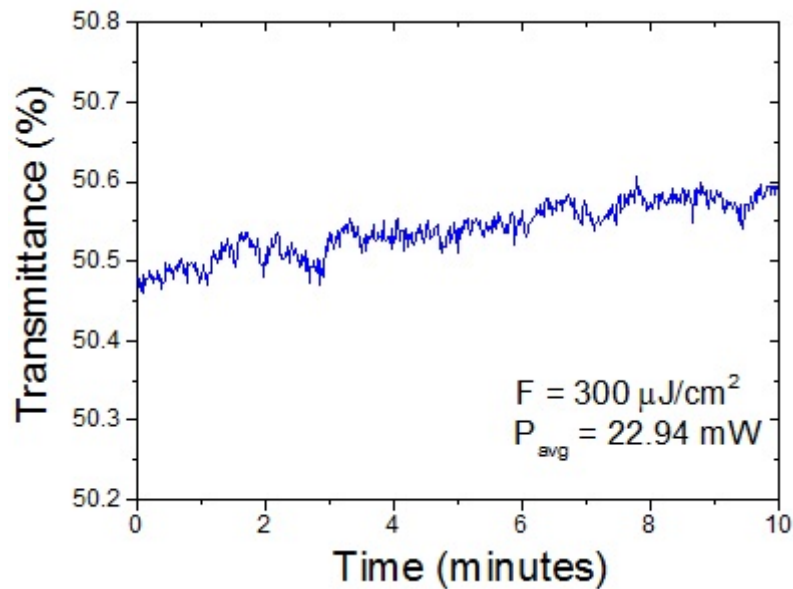
Figure 3.29: Change in transmittance with time of graphene film sandwiched between two quartz slides, exposed to a pulsed laser at an average power of 14.60mW $(300\mu J/cm^2)$.
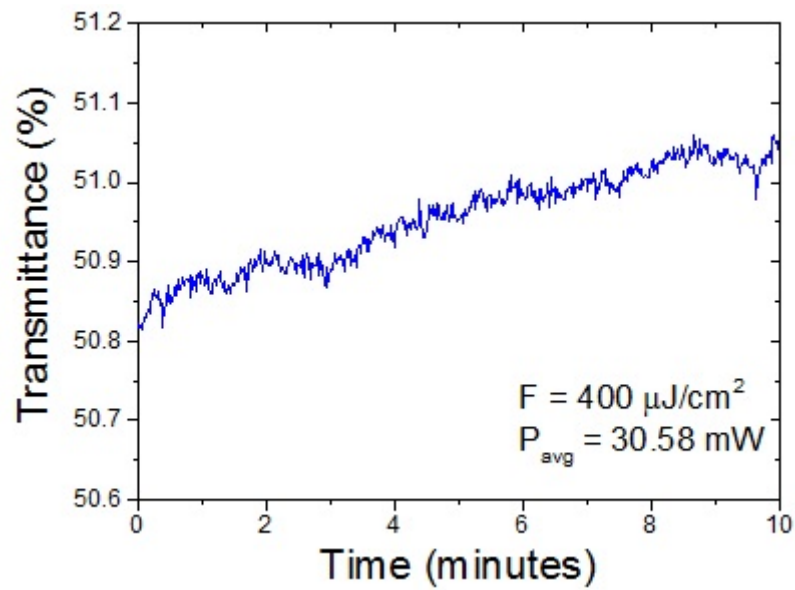
Figure 3.30: Change in transmittance with time graphene film sandwiched between two quartz slides, exposed to a pulsed laser at an average power of 19.47mW (400μJ/cm^2).
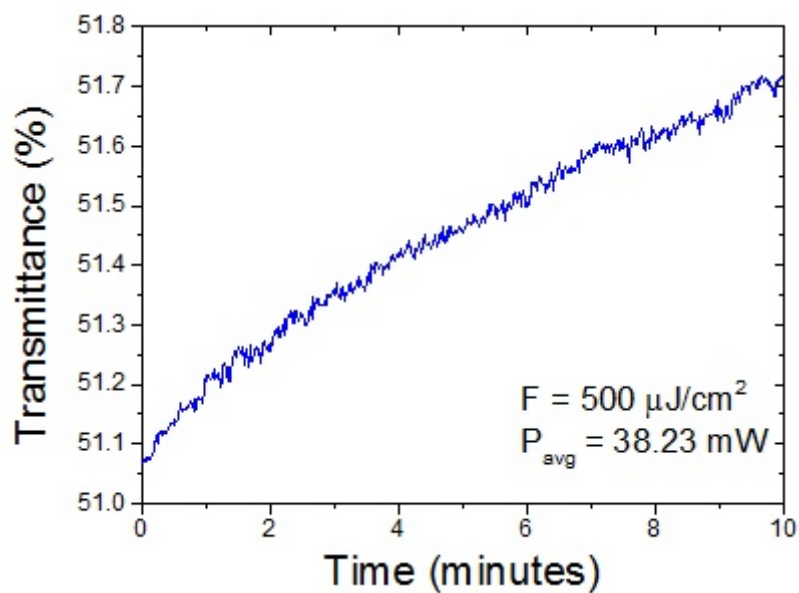
Figure 3.31: Change in transmittance with time of graphene film sandwiched between two quartz slides, exposed to a pulsed laser at an average power of 24.34mW (500μJ/cm^2).

Starting from a fluence of 500 μ J / cm^2 a relevant change in transmittance, approximately 0.6% occurs during the exposure period. Moreover, the change in transmittance it is permanent, that is it does not recover when the laser source is shut down. This modification could be attributed to a degradation of the graphene film, although a specific mechanism cannot be proposed. It is also important to state that this partial damage may still allow the operation of the graphene SA: the graphene film still shows modulation of the transmittance with intensity, and fibre lasers are not significantly susceptible to such low variations on insertion losses.

I now present the results of the nonlinear transmittance measurements carried on the graphene-PVA composite with the same setup as above. First of all it is important to state that this time the graphene SA was not sandwiched between two quartz slides because of the sample thickness (approximately 50 μm): as a matter of fact, such expedient would have been equivalent to placing a resonant cavity along the beam line. The bare graphene-PVA composite was then secured in a suitable position by a holder.
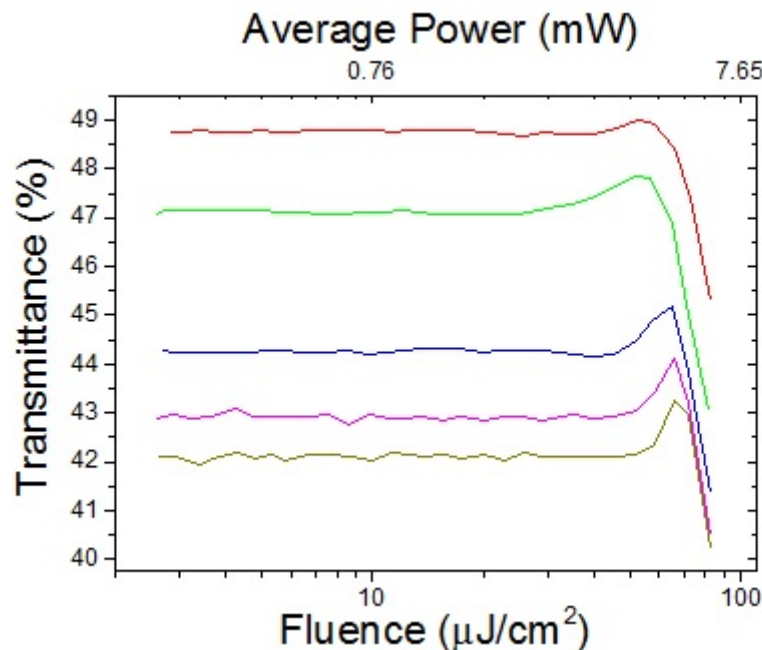
Figure 3.32: Nonlinear transmittance measurements carried consecutively on a bare piece of graphene-PVA composite.

From the Figure above, a behaviour similar to that shown in Figure 3.22 is recognisable: the initial increase in transmittance is most likely due to saturation of absorption, followed by a dramatic drop. I again attribute this drop in

transmittance to the onset of a damage process. Figures 3.32 shows the result of subsequent measurements: the initial baseline progressively shifts towards lower transmittance values, and I attribute this behaviour to a progressive deterioration of the composite.

Chapter 4

Laser operation and mode-locking results

In this chapter I will present the fibre laser adopted for the graphene SA testing, which is equivalent to that used in Ref. [53]. Moreover, I will demonstrate ultra-fast pulse generation in a power scaling laser, with a maximum intracavity power level higher than what has been reported in literature for graphene-polymer composites [8].

4.1 Fibre laser cavity

Fibre lasers have shown a tremendous progress in recent years: the increase in number of applications is driven by the fact that they can reach same or better performances, when compared to bulk lasers, at much lower costs. Indeed, fibre lasers attractiveness is justified by their simple and compact design, efficient heat dissipation and alignment-free operation. Fibre lasers typically adopt a gain medium based on rare-earth-doped fibres such as Ytterbium (Yb^{3+}), Neodymium (Nd^{3+}), Erbium (Er^{3+}), Thulium (Tm^{3+}) or Holmium (Ho^{3+}), and they are usually pumped by one or more laser diodes. A typical approach to ultrafast pulse generation in fibre lasers relies on Soliton ML, described in section 2.2.2, with the aid of a SA [47][1] [18] [17] [60].

The schematics of the fibre laser cavity used are shown in Figure 4.1. The gain medium is a 3m EDF (Fibercore EDF M-5) with $\beta_2 = 22.35\text{ps}^2/\text{km}$, while the rest of the cavity consists of 6.2m single mode fibre SMF-28 with $\beta_2 = -22.87\text{ps}^2/\text{km}$, in order to obtain the overall negative dispersion that is necessary for Soliton formation in the cavity. The EDF is pumped by a 980nm laser diode (LD) through a wavelength division multiplexer (WDM). Unidirectional lasing in the ring is achieved with an optical isolator (ISO). The laser
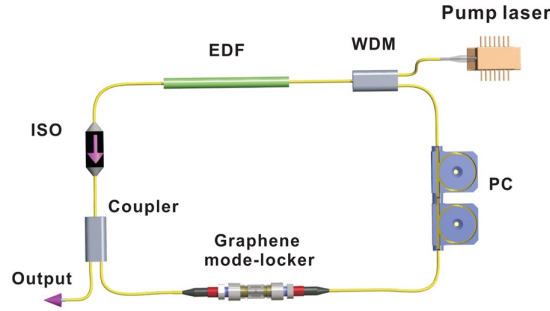
Figure 4.1: Fibre laser cavity. Adapted from Ref. [53]

output is directed through the 20% port of a coupler. For mode-locking optimisation, a polarisation controller (PC) is placed after the SA. The total cavity length is approximately 9.2m.

4.2 Mode-locking results: graphene film

Among the graphene film samples presented in Table 3.2, the 160 μl was successful in inducing mode-locking. The laser output was characterised with different techniques:

Optical spectrum
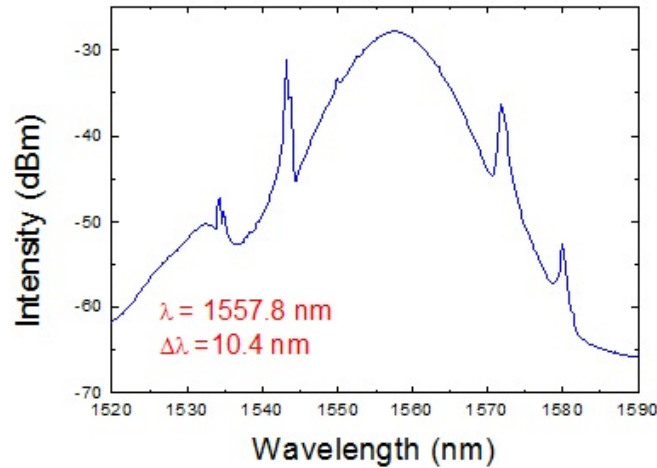
Figure 4.2: Optical spectrum of a pulse generated by a fibre laser, mode-locked by a graphene film SA.

Figure 4.2 shows the optical spectrum of the laser pulses, which are centred at 1557.8nm. The two evident sidebands situated at approximately 1543.2nm and 1571.8nm are expected for Soliton ML [56]. The FWHM bandwidth of the spectrum is 10.4nm.

Autocorrelation trace

Figure 4.3 plots the SHG autocorrelation trace. For a sech^2 profile, a pulse duration of 238fs was measured.
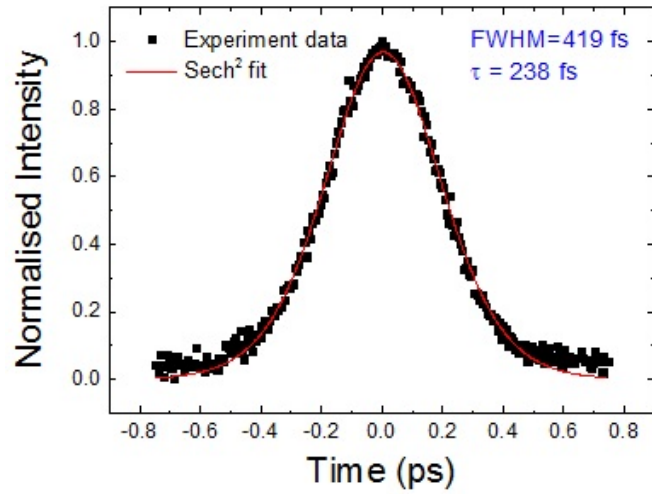
Figure 4.3: Autocorrelation trace of a pulse generated by a fibre laser, mode-locked by a graphene film SA.

Oscilloscope trace
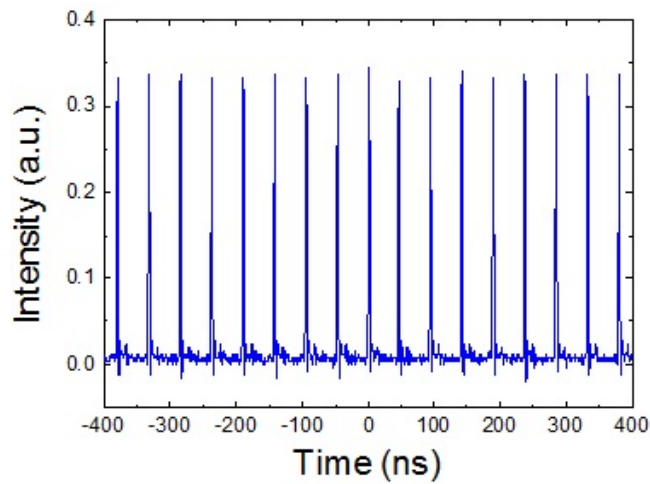
Figure 4.4: Oscilloscope trace of a pulse-train generated by a fibre laser, mode-locked by a graphene film SA.

The oscilloscope trace (Figure 4.4) is obtained by using a photodetector connected to an oscilloscope. The time interval between pulses is approximately 47.6ns corresponds to the cavity round trip time which is consistent with the measured cavity length.

RF spectrum
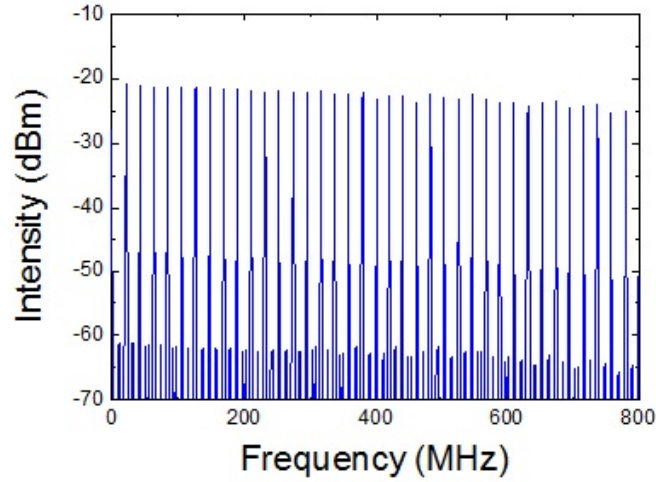
Figure 4.5: Wide RF spectrum obtained by coupling the laser output to a photodetector connected to an RF spectrum analyser.

The RF spectrum is recorded by using a photodetector connected to a RF spectrum analyser. In Figure 4.5 the RF spectrum is presented over a wide interval of frequencies (resolution bandwidth 30Hz): around the fundamental repetition rate ($f_1 = 21.06$MHz), the signal-to-noise ratio (SNR) is greater than 80dB (Figure 4.6).
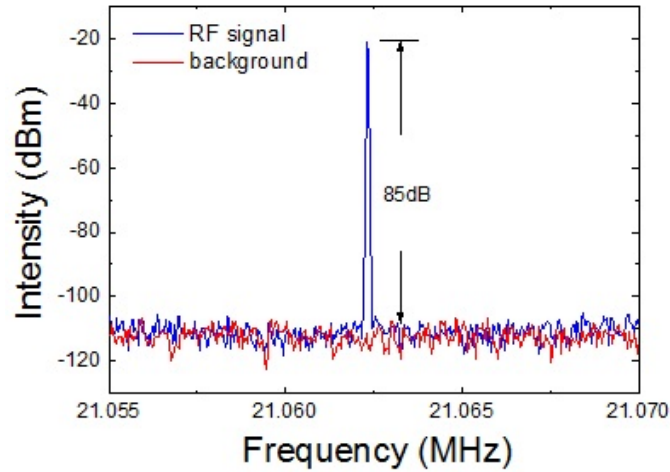
Figure 4.6: RF spectrum centred around the fundamental repetition rate: $f_1 = 21.06$MHz.

This significant SNR implies low-amplitude fluctuations of the laser, thus confirming the stability of the mode-locking regime [59], an important factor for applications.

Power scaling

Figure 4.7 shows that mode-locked operation can be continuously maintained up to a pump power of 350mW, which corresponds to an output power of approximately 16mW and to an intracavity power of approximately 80mW. The output, which scales linearly with the pump power, is limited by the maximum power of our pump laser diode, and it could be possible to increase the output level by using a different pump laser.
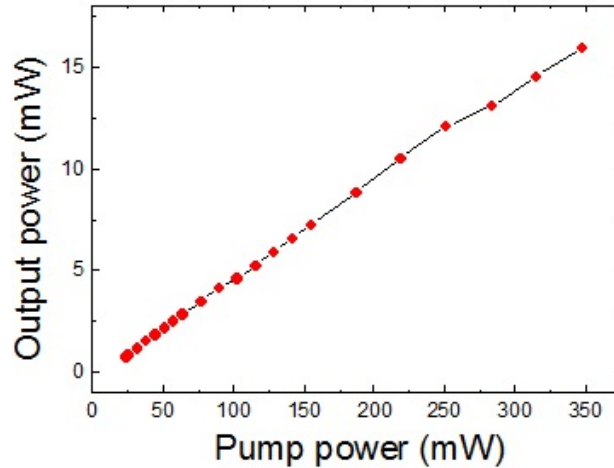
Figure 4.7: Fibre laser cavity. Adapted from Ref. [53]

This results seems to further support the considerations made in section 3.4.2 regarding the superior stability of graphene film at high power level, compared to graphene-PVA composites. Reference [8] reports the most relevant recent results obtained with graphene SA in Erbium Doped Fibre Lasers.

Laser type	Coupling method	Fabrication method	λ (nm)	Laser parameters τ	f(MHz)	P(mw)	Ref.
Graphene							
EDFL	Sandwiching	LPE	1557	800fs	//	//	[5]
			1559	464fs	19.9	1	[20]
			1525 − 1559 Tunable	1ps	8	1	[10]
			1560	174fs	27.4	1.2	[112]
			1560	630fs	19.9	//	[66]
			1532	850fs	5.27	//	[122]
			1562	865fs	9.67GHz	316	[123]
			Four-λ ($\sim$ 1530)	8.8ps	8.03	3.56	[128]
			1560	1ps	13.6	3.7	[132]
			1565	190fs	42.8	0.4	[133]
		FG	1570 − 1560 Tunable	1.08ps	6.95	//	[82]
		GO	1596	770fs	21.79	0.85	[134]
		RGO	1590	694fs	6.95	50	[120]
			1560	18ps	7.47	1.2	[135]
			1562	938fs	15.2	4.1	[136]
			1562	950fs	502.8	2.3	[137]
			1560	1.64, 9.15ps	2.57, 7.05	//	[138]
			1572	//	91.5	//	[84]

Figure 4.8: Review of the results obtained up to 2014 with graphene SAs in Erbium Doped Fibre Lasers. Adapted from Ref. [8]

The cavity used in this work shows an intracavity power second only to Ref. [65] (Ref. 120 in Figure 4.8 in the field of graphene film SA obtained by LPE sandwiched in a EDF ring-cavity laser. Zhang et al. made use of a different polymer to form the composite (PVDF, i.e. Polyvinylidene Fluoride). The 316mW obtained by Martinez et al. (Ref. 123 in Figure 4.8) were measured in a very different laser cavity compared to that shown in Figure 4.1, and the graphene SA was deposited in the cavity by spraying the graphene dispersion on a fibre mirror [40].

Chapter 5

Related experiments

In the previous two chapters, I presented a novel method for integrating a graphene SA into a fibre laser cavity. The rationale behind this newly developed technique, which makes use of a piece of graphene film rather than a graphene-PVA composite, is to obtain a photonic device capable of withstanding high power levels with respect to previous works on graphene SAs.

In chapter 3, section 3.4.2, I showed evidence of the superior performance of graphene films with respect to graphene-PVA composites in terms of stability when exposed to intense laser light. Moreover, in chapter 4, the excellent power scaling capabilities of the fibre laser cavity employing a graphene film SA were demonstrated.

In this chapter I will show an alternative integration method that was attempted in order to reach even higher power levels without damaging the SA. Contrarily to the previous one, this approach was not successful, however further work in this direction could lead to important results.

5.1 Graphene film transfer on a D-shaped fibre

Figure 5.1 shows a representation of a D-shaped fibre, i.e. an ordinary optical fibre which has been polished in order to partially expose the core of the waveguide. This device is particularly interesting for our application because it is possible to deposit the graphene SA on the flat surface of the polished fibre: this approach relies on the interaction of the evanescent field of the light beam, travelling along the core of the fibre, with the graphene planes deposited parallel to the light propagation direction. The potential advantages of this technique, with respect to the transfer of the graphene film on the tip of the fibre connector, are related to the fact that the SA does not contribute significantly to the linear losses in the cavity, and it would be less affected by high optical powers.

Figure 5.1: Deposition of a graphene SA on a D-shaped fibre. Adapted from Ref. [39]

Figures 5.2 and 5.3 presents the D-shaped fibre before and after the transfer of the graphene film, respectively. The process employed is equivalent to that discussed in section 3.2.2.
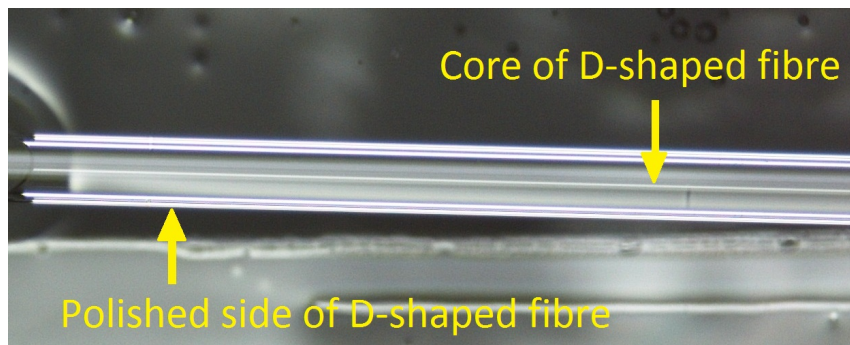
Figure 5.2: Dark field microscope image (5x) of a clean D-shaped fibre.
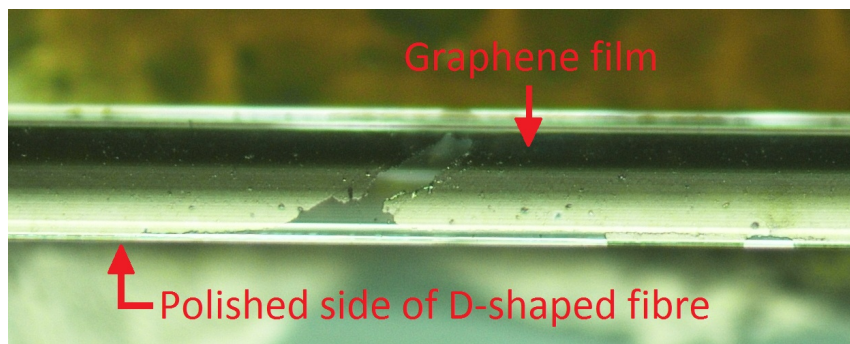
Figure 5.3: Microscope image (10x) of a D-shaped fibre on which a piece of Graphene Flm has been transferred.

The nonlinear transmittance modulation of these sample is still under investigation.

Chapter 6

Conclusions and perspectives

This thesis focuses on the development of fast broadband graphene SAs, intended for a fibre laser cavity operating at 1550nm. These photonic devices were produced using Liquid Phase Exfoliation: this approach had been successfully employed in previous studies by embedding the graphene in a polymer matrix. The composite material thus produced has excellent performances and it is particularly easy to integrate it in the fibre laser cavity; however, the presence of the polymer within the laser cavity may raise some issues in terms of the maximum optical power sustainable by the SA. For this reason, object of this work was to develop a new polymer-free integration technique, able to maintain or increase the performances of the laser with respect to the results reported in literature.

In the following chapter I will present a summary of the work done and of the results of the characterisation and integration of the graphene film SA; in particular, experimental evidence of the success of the novel polymer-free integration technique will be highlighted. I shall also give a perspective on future investigations in this field.

6.1 Summary of work done: graphene film preparation and integration in a fibre laser cavity

Graphene dispersion preparation

The starting water-based graphene dispersion was prepared following the procedure explained in section 3.1, obtaining a final concentration of 0.235g/l, as it was ascertained by Optical Absorption Spectroscopy. Multi-wavelength Raman Spectroscopy was carried on the dispersion by drop-casting it on a Si/SiO_2 substrate, followed by a statistical analysis of the Raman spectra acquired.

Graphene SA preparation

The graphene dispersion characterisation was followed by the graphene film production through vacuum filtration. The setup shown in Figure 3.9 was utilized to prepare films of different thickness and, consequently, of different transmittance. The graphene films were first transferred on a quartz substrate and then optically characterised with two different setups in order to determine their linear and nonlinear optical properties; their average thickness was also measured with a profilometer. The same graphene dispersion was also used to produce a graphene-PVA composite, following the same process developed by Reference [27]. The two types of graphene SA, the film and the composite, were hence tested in the two available laser setups in order to assess their performance and behaviour when exposed to high optical power.

Graphene SA integration

A transfer technique was developed and subsequently used to place a piece of each graphene film on the tip of a fibre connector. The sample was then placed in a EDF laser cavity, and mode-locking regime was attained and fully characterised.

6.2   Summary of results

Graphene dispersion characterisation

The results of the characterisation of the graphene dispersion are reported in section 3.1. The Optical Absorption Spectroscopy measurements indicate a concentration on graphene in solution of approximately 0.235g/l, while the doping $(0.5 \times 10^{13} \mathrm{cm}^{-2})$ and the sp^3 (0%) content of the graphene was assessed though Raman spectroscopy.

Graphene film characterisation

The graphene films were transferred on two different types of substrate: quartz slides and optical fibre connectors. Their optical properties were characterised with a UV-Vis spetrometer in order to determine the linear absorption. The films, as expected, show a featureless absorption spectrum apart for a peak at 270nm due to the Van Hove singularity in the DOS of graphene. The nonlinear optical absorption was assessed using two different setups, shown in Figures 2.31 and 2.32. The results show a discrete modulation of transmittance as a function of laser intensity (approximately 5%). Moreover, the same setups

were used to determine whether the graphene films were actually more stable than the graphene-PVA composites when exposed to high optical power: the results seem to suggest that the films have indeed an improved resistance to optical damage, although further investigation should provide a model for the degradation mechanism of the composite.

Graphene SA integration and laser characterisation

The graphene SAs placed on the tip of the fibre connectors were inserted in a EDF laser cavity. Stable mode-locking regime was observed, and the sub-250fs laser pulses (repetition rate of 21MHz) were characterised with an optical spectrum analyser, an autocorrelator, an oscilloscope and a RF spectrum analyser. More importantly, continuous ultrafast pulse generation was reported at very different pumping power levels (see Figure 4.7): the excellent power scaling capabilities of the laser cavity seem to further support our claim that the graphene films are less vulnerable to high optical powers compared to the graphene-PVA composites.

6.3   Perspectives on future progresses

Graphene is a material that presents a wealth of interesting optical, mechanical and transport properties that have inevitably posed it under the intense attention of the Research community. The world of photonics, among others, is particularly keen in exploiting the peculiar absorption characteristic of this material for various applications, from photo-detectors and Terahertz devices to transparent conductors and plasmonic devices. In this work I have presented a progress in the field of graphene Saturable Absorbers, i.e. I have developed a technique that could possibly extend the application of graphene SAs, an already well established technology at research level, to laser cavities operating at higher optical power.

Further works could follow the approach attempted in chapter 5 with D-shaped fibres, for example by choosing a more appropriate deposition techniques of graphene on the active surface of the fibre. Indeed, a very promising deposition technique is spray-coating: apart for the tremendous advantages in terms of cost and scalability of such process, this method, if properly optimised, allows a very even, precise and fast deposition of the material on the substrate.

Other possible works in this fields could include the use of other layered materials, such as MoS_2 and other TMDs (Transition Metal Dichalcogenenides): the former, for example, shows a direct bandgap only when it is isolated in the

form of a monolayer, and excellent saturable absorption responses have been reported by Reference [61].

Appendix A

Mode-locking results: graphene-PVA composite

In section 3.4.2 a piece of graphene-PVA composite was used to evaluate the improved optical stability of the graphene film with respect to the graphene-PVA composite. Moreover, in chapter 4 I presented the mode-locking results for the graphene film SA integrated in the Erbium Doped Fibre Laser cavity.

In the graphs below I present the optical and RF spectra for the graphene-PVA composite, as they were obtained by integrating the SA in the same laser cavity described in chapter 4.
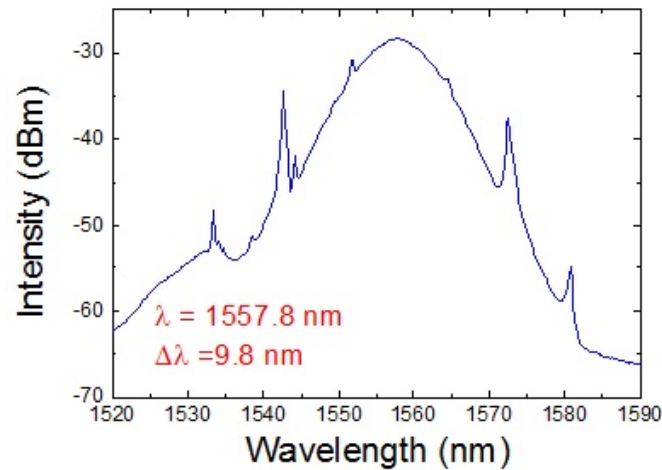

Figure A.1: Optical spectrum of a pulse generated by a fibre laser, mode-locked by a graphene film SA.
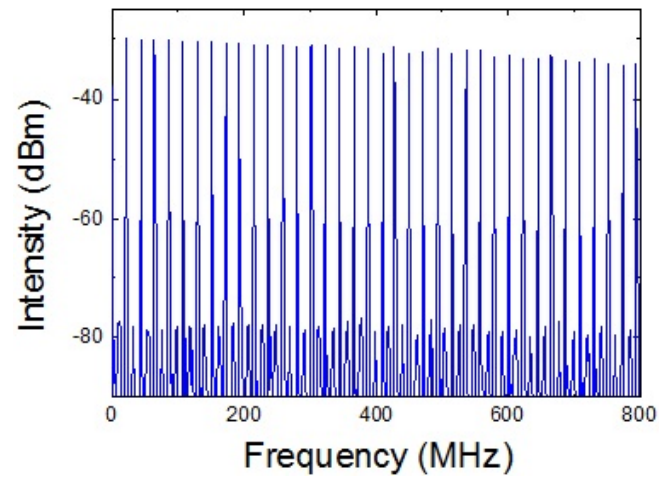
Figure A.2: Wide RF spectrum obtained by coupling the laser output to a photodetector connected to an RF spectrum analyser.

Bibliography

[1] G. P. Agrawal. *Nonlinear fiber optics.* Springer, 2000.

[2] N. Ashcroft and N. Mermin. *Solid State Physics.* Saunders College, Philadelphia, 1976.

[3] S. Bae, H. Kim, Y. Lee, X. Xu, J.-S. Park, Y. Zheng, J. Balakrishnan, T. Lei, H. R. Kim, Y. I. Song, et al. Roll-to-roll production of 30-inch graphene films for transparent electrodes. *Nature nanotechnology*, 5(8):574–578, 2010.

[4] Q. Bao, H. Zhang, Y. Wang, Z. Ni, Y. Yan, Z. X. Shen, K. P. Loh, and D. Y. Tang. Atomic-layer graphene as a saturable absorber for ultrafast pulsed lasers. *Advanced Functional Materials*, 19(19):3077–3083, 2009.

[5] D. M. Basko, S. Piscanec, and A. C. Ferrari. Electron-electron interactions and doping dependence of the two-phonon raman intensity in graphene. *Phys. Rev. B*, 80:165413, Oct 2009.

[6] F. Bonaccorso. PhD thesis, University of Messina, 2009.

[7] F. Bonaccorso, A. Lombardo, T. Hasan, Z. Sun, L. Colombo, and A. C. Ferrari. Production and processing of graphene and 2d crystals. *Materials Today*, 15(12):564 – 589, 2012.

[8] F. Bonaccorso and Z. Sun. Solution processing of graphene, topological insulators and other 2d crystals forultrafast photonics. *Opt. Mater. Express*, 4(1):63–78, Jan 2014.

[9] F. Bonaccorso, Z. Sun, T. Hasan, and A. C. Ferrari. Graphene photonics and optoelectronics. *Nature Photonics*, 4(9):611–622, 2010.

[10] R. W. Boyd. *Nonlinear optics.* Academic press, 2003.

[11] M. Breusing, S. Kuehn, T. Winzer, E. Malić, F. Milde, N. Severin, J. P. Rabe, C. Ropers, A. Knorr, and T. Elsaesser. Ultrafast nonequilibrium carrier dynamics in a single graphene layer. *Phys. Rev. B*, 83:153410, Apr 2011.

[12] D. Brida, C. Manzoni, G. Cerullo, A. Tomadin, M. Polini, R. R. Nair, A. K. Geim, K. S. Novoselov, S. Milana, A. Lombardo, et al. Ultrafast non-thermal electron dynamics in single layer graphene. In *EPJ Web of Conferences*, volume 41, page 04025. EDP Sciences, 2013.

[13] D. Brida, A. Tomadin, C. Manzoni, Y. J. Kim, A. Lombardo, S. Milana, R. R. Nair, K. S. Novoselov, A. C. Ferrari, G. Cerullo, et al. Ultrafast collinear scattering and carrier multiplication in graphene. *Nature communications*, 4, 2013.

[14] C. Casiraghi, A. Hartschuh, E. Lidorikis, H. Qian, H. Harutyunyan, T. Gokus, K. Novoselov, and A. C. Ferrari. Rayleigh imaging of graphene and graphene layers. *Nano letters*, 7(9):2711–2717, 2007.

[15] A. Das, S. Pisana, B. Chakraborty, S. Piscanec, S. Saha, U. Waghmare, K. Novoselov, H. Krishnamurthy, A. Geim, A. Ferrari, et al. Monitoring dopants by raman scattering in an electrochemically top-gated graphene transistor. *Nature nanotechnology*, 3(4):210–215, 2008.

[16] S. De, P. J. King, M. Lotya, A. O'Neill, E. M. Doherty, Y. Hernandez, G. S. Duesberg, and J. N. Coleman. Flexible, transparent, conducting films of randomly stacked graphene from surfactant-stabilized, oxide-free graphene dispersions. *Small*, 6(3):458–464, 2010.

[17] M. J. Digonnet. *Rare-earth-doped fiber lasers and amplifiers, revised and expanded*. CRC press, 2002.

[18] M. E. Fermann, A. Galvanauskas, and G. Sucha. *Ultrafast lasers: Technology and applications*, volume 80. CRC Press, 2002.

[19] A. C. Ferrari. Raman spectroscopy of graphene and graphite: Disorder, electron–phonon coupling, doping and nonadiabatic effects. *Solid State Communications*, 143(1–2):47 – 57, 2007. Exploring graphene Recent research advances.

[20] A. C. Ferrari and D. M. Basko. Raman spectroscopy as a versatile tool for studying the properties of graphene. *Nature nanotechnology*, 8(4):235–246, 2013.

[21] A. C. Ferrari, J. C. Meyer, V. Scardaci, C. Casiraghi, M. Lazzeri, F. Mauri, S. Piscanec, D. Jiang, K. S. Novoselov, S. Roth, et al. Raman spectrum of graphene and graphene layers. *Physical review letters*, 97(18):187401, 2006.

[22] A. C. Ferrari and J. Robertson. Interpretation of raman spectra of disordered and amorphous carbon. *Phys. Rev. B*, 61:14095–14107, May 2000.

[23] A. C. Ferrari and J. Robertson. Resonant raman spectroscopy of disordered, amorphous, and diamondlike carbon. *Phys. Rev. B*, 64:075414, Jul 2001.

[24] A. K. Geim and K. S. Novoselov. The rise of graphene. *Nature materials*, 6(3):183–191, 2007.

[25] C. M. Hansen. *Hansen solubility parameters: a user's handbook.* CRC press, 2012.

[26] T. Hasan, Z. Sun, F. Wang, F. Bonaccorso, P. H. Tan, A. G. Rozhin, and A. C. Ferrari. Nanotube–polymer composites for ultrafast photonics. *Advanced Materials*, 21(38-39):3874–3899, 2009.

[27] T. Hasan, F. Torrisi, Z. Sun, D. Popa, V. Nicolosi, G. Privitera, F. Bonaccorso, and A. C. Ferrari. Solution-phase exfoliation of graphite for ultrafast photonics. *physica status solidi (b)*, 247(11-12):2953–2957, 2010.

[28] Y. Hernandez, V. Nicolosi, M. Lotya, F. M. Blighe, Z. Sun, S. De, I. McGovern, B. Holland, M. Byrne, Y. K. Gun'Ko, et al. High-yield production of graphene by liquid-phase exfoliation of graphite. *Nature Nanotechnology*, 3(9):563–568, 2008.

[29] F. Kartner, I. Jung, and U. Keller. Soliton mode-locking with saturable absorbers. *Selected Topics in Quantum Electronics, IEEE Journal of*, 2(3):540–556, 1996.

[30] U. Keller. Recent developments in compact ultrafast lasers. *Nature*, 424(6950):831–838, 2003.

[31] U. Keller. Ultrafast solid-state lasers. volume 46 of *Progress in Optics*, pages 1 – 115. Elsevier, 2004.

[32] V. G. Kravets, A. N. Grigorenko, R. R. Nair, P. Blake, S. Anissimova, K. S. Novoselov, and A. K. Geim. Spectroscopic ellipsometry of graphene and an exciton-shifted van hove peak in absorption. *Phys. Rev. B*, 81:155413, Apr 2010.

[33] A. Kuzmenko, E. Van Heumen, F. Carbone, and D. Van Der Marel. Universal optical conductance of graphite. *Physical review letters*, 100(11):117401, 2008.

[34] R. B. Laughlin. Graphene density of states, 2008.

[35] D. R. Lide. 86th handbook of chemistry and physics, 2006.

[36] M. Lotya, Y. Hernandez, P. J. King, R. J. Smith, V. Nicolosi, L. S. Karlsson, F. M. Blighe, S. De, Z. Wang, I. T. McGovern, G. S. Duesberg, and J. N. Coleman. Liquid phase production of graphene by exfoliation of graphite in surfactant/water solutions. *Journal of the American Chemical Society*, 131(10):3611–3620, 2009.

[37] D. J. Maas, B. Rudin, A.-R. Bellancourt, D. Iwaniuk, S. V. Marchese, T. Südmeyer, and U. Keller. High precision optical characterization of semiconductor saturable absorber mirrors. *Opt. Express*, 16(10):7571–7579, May 2008.

[38] A. Martinez, K. Fuse, and S. Yamashita. Mechanical exfoliation of graphene for the passive mode-locking of fiber lasers. *Applied Physics Letters*, 99(12), 2011.

[39] A. Martinez and Z. Sun. Nanotube and graphene saturable absorbers for fibre lasers. *Nature Photonics*, 7(11):842–845, 2013.

[40] A. Martinez and S. Yamashita. 10ghz fundamental mode fiber laser using a graphene saturable absorber. *Applied Physics Letters*, 101(4), 2012.

[41] K. Miyajima, K. Machida, T. Taga, H. Komatsu, and M. Nakagaki. Correlation between the hydrophobic nature of monosaccharides and cholates, and their hydrophobic indices. *Journal of the Chemical Society, Faraday Transactions 1: Physical Chemistry in Condensed Phases*, 84(8):2537–2544, 1988.

[42] R. R. Nair, P. Blake, A. N. Grigorenko, K. S. Novoselov, T. J. Booth, T. Stauber, N. M. R. Peres, and A. K. Geim. Fine structure constant defines visual transparency of graphene. *Science*, 320(5881):1308–1308, 2008.

[43] A. H. C. Neto, F. Guinea, N. M. R. Peres, K. S. Novoselov, and A. K. Geim. The electronic properties of graphene. *Reviews of modern physics*, 81(1):109, 2009.

[44] K. S. Novoselov, V. I. Fal, L. Colombo, P. R. Gellert, M. Schwab, and K. Kim. A roadmap for graphene. *Nature*, 490(7419):192–200, 2012.

[45] K. S. Novoselov, D. Jiang, F. Schedin, T. J. Booth, V. V. Khotkevich, S. V. Morozov, and A. K. Geim. Two-dimensional atomic crystals. *Proceedings of the National Academy of Sciences of the United States of America*, 102(30):10451–10453, 2005.

[46] S. Piscanec, M. Lazzeri, F. Mauri, A. C. Ferrari, and J. Robertson. Kohn anomalies and electron-phonon interactions in graphite. *Phys. Rev. Lett.*, 93:185503, Oct 2004.

[47] D. Popa, Z. Sun, F. Torrisi, T. Hasan, F. Wang, and A. Ferrari. Sub 200 fs pulse generation from a graphene mode-locked fiber laser. *Applied Physics Letters*, 97(20):203106, 2010.

[48] A. Reina, S. Thiele, X. Jia, S. Bhaviripudi, M. S. Dresselhaus, J. A. Schaefer, and J. Kong. Growth of large-area single-and bi-layer graphene by controlled carbon precipitation on polycrystalline ni surfaces. *Nano Research*, 2(6):509–516, 2009.

[49] A. Roda, A. F. Hofmann, and K. J. Mysels. The influence of bile salt structure on self-association in aqueous solutions. *Journal of Biological Chemistry*, 258(10):6362–70, 1983.

[50] V. Scardaci, Z. Sun, F. Wang, A. G. Rozhin, T. Hasan, F. Hennrich, I. H. White, W. I. Milne, and A. C. Ferrari. Carbon nanotube polycarbonate composites for ultrafast lasers. *Advanced Materials*, 20(21):4040–4043, 2008.

[51] P. Schuck. Size-distribution analysis of macromolecules by sedimentation velocity ultracentrifugation and lamm equation modeling. *Biophysical journal*, 78(3):1606–1619, 2000.

[52] Z. Sun, T. Hasan, and A. C. Ferrari. Ultrafast lasers mode-locked by nanotubes and graphene. *Physica E: Low-dimensional Systems and Nanostructures*, 44(6):1082–1091, 2012.

[53] Z. Sun, T. Hasan, F. Torrisi, D. Popa, G. Privitera, F. Wang, F. Bonaccorso, D. M. Basko, and A. C. Ferrari. Graphene mode-locked ultrafast laser. *Acs Nano*, 4(2):803–810, 2010.

[54] T. Svedberg, K. O. Pedersen, et al. The ultracentrifuge. *The Ultracentrifuge.*, 1940.

[55] O. Svelto. *Principles of lasers.* 1976.

[56] K. Tamura, L. Nelson, H. Haus, and E. Ippen. Soliton versus nonsoliton operation of fiber ring lasers. *Applied physics letters*, 64(2):149–151, 1994.

[57] A. Tomadin, D. Brida, G. Cerullo, A. C. Ferrari, and M. Polini. Nonequilibrium dynamics of photoexcited electrons in graphene: Collinear scattering, auger processes, and the impact of screening. *Phys. Rev. B*, 88:035430, Jul 2013.

[58] F. Torrisi. *Nanomaterials-based dispersions, inks and composites for flexible electronics and photonics.* PhD thesis, University of Cambridge, 2012.

[59] D. von der Linde. Characterization of the noise in continuously operating mode-locked lasers. *Applied Physics B*, 39(4):201–217, 1986.

[60] F. Wang, A. Rozhin, V. Scardaci, Z. Sun, F. Hennrich, I. White, W. I. Milne, and A. C. Ferrari. Wideband-tuneable, nanotube mode-locked, fibre laser. *Nature nanotechnology*, 3(12):738–742, 2008.

[61] K. Wang, J. Wang, J. Fan, M. Lotya, A. O'Neill, D. Fox, Y. Feng, X. Zhang, B. Jiang, Q. Zhao, H. Zhang, J. N. Coleman, L. Zhang, and W. J. Blau. Ultrafast saturable absorption of two-dimensional mos2 nanosheets. *ACS Nano*, 7(10):9260–9267, 2013.

[62] J. W. Williams, K. E. Van Holde, R. L. Baldwin, and H. Fujita. The theory of sedimentation analysis. *Chemical Reviews*, 58(4):715–744, 1958.

[63] H.-S. P. Wong and D. Akinwande. *Carbon nanotube and graphene device physics.* Cambridge University Press, 2011.

[64] G. Xing, H. Guo, X. Zhang, T. C. Sum, and C. H. A. Huan. The physics of ultrafast saturable absorption in graphene. *Opt. Express*, 18(5):4564–4573, Mar 2010.

[65] H. Zhang, Q. Bao, D. Tang, L. Zhao, and K. Loh. Large energy soliton erbium-doped fiber laser with a graphene-polymer composite mode locker. *Applied Physics Letters*, 95(14):141103, 2009.